POLITECNICO DI TORINO

ENGINEERING SCHOOL
Master Degree in Mathematical Engineering

Thesis

# Mesh quality effects on the simulated flow around a square cylinder: a computational study


**Advisors**
Luca Bruno
Domenic D'Ambrosio

**Author**
Andrea Bianco

July 2018

# Summary

In this Thesis it is showed a study about the effects that a poor quality mesh has in the solution of a computational simulation. There are many problems in Fluid Dynamics that can not be solved analytically. So, *Computational Fluid Dynamics* allows us to have a numerical result. The wide range of applications, and its lower cost in comparison with the experimental process are examples of advantages of CFD, so that the non-existent limit to the structural dimensions of what we would like to simulate and the time of computation that is related to the computers. However, disadvantages are present. We could make mistakes about setting parameters, building physical models in wrong way. Moreover we could make wrong interpretation of the results if we don't have real perspectives about what we are simulating. So, it is very important to verify the appropriate definition of all parameters and variables of our problem in order to get a suitable solution, and finally, we have to correctly interpret the results so that we could make correct decisions in our application.

The present Thesis investigates the effect of the mesh quality because of its influences in the result. There are many types of error with several effects in the solution. In particular, grid quality error needs to be explained. The study consists to compare seven different types of meshes in a fluid flow around a square cylinder. All seven grids are very similar, except on the near region where the boundary layer is present. So, each mesh has a concrete and distinct value of grid quality. After the simulation, we will discuss the results of the various cases between them. It has been demonstrated that the error propagated by an inadequate definition of the parameters of the grid quality is significant. The real magnitude of this effect is relative to the force modulus and its application. For example, in the field of Civil Engineering, an error in the calculation of the structure of a building could have catastrophic consequences.

Finally, the outline of this Thesis gives a concrete idea what each chapter is about and shows schematically the evolutionary process which has taken place during its development.

**Chapter 1** introduces the *Computational Wind Engineering*, field in which this study is involved. In particular, the problem of the square cylinder is shown.

**Chapter 2** is an overview about several articles in which some CWE or CFD simulations about flow around a square cylinder, or similar problems, are studied and compared with the bibliography, giving us some references to our results.

**Chapter 3** numerical methods in CWE are introduced. The base concepts of Fluid Dynamics are explained in order to comprehend the physical concepts of a simulation problem.

**Chapter 4** explains the methodology to grid generation. In particularly, notions of grid quality errors and their relation to the solution are clarified.

**Chapter 5** describes the steps in order build the model in the program and run the simulation. In addition, there are described the seven cases of study.

**Chapter 6** discuss all results obtained after the simulation for each case. The effects of the mesh quality will be verified analyzing the change on the solutions for each grid type.

Finally, **Chapter 7** summarizes the main result of this Thesis after discussing the solutions for each different grids. Moreover, new problems for future works and applications of these results are explained.

In conclusion, this Thesis provides a systematic study about the effects of mesh quality in the numerical solutions, that can be a wide application in the *Computational Wind Engineering*.

# Contents

# List of Figures

# List of Tables

# Chapter 1

# Introduction

In physics, *Computational Fluid Dynamics* (CFD) is the branch of Fluid Fynamics that provides a cost-effective means of simulating real flows by the numerical solution of the governing equations, that for Newtonian fluid dynamics are named the Navier-Stokes equations. However, the development of reduced forms of these equations is still an active field of research. In particular, the turbulent closure problem of the Reynold-average Navier-Stokes equations.

The most reliable information about physical phenomena is usually given by measurements. However, in many situations, measuring equipment can have significant errors. So, the need for reliable computational models is of great importance, and required validation using experimental data before they can be put to a validation. In this Thesis, we focus on using the Computational Fluid Dynamics for wind engineering applications, *Computational Wind Engineering* (CWE). The main objective of this study is to show a direct relation between the solution errors and a bad quality mesh. However, it is needed to learn about the interaction between the fluid and the square cylinder.

The square cylinder, or also the rectangular cylinder where, in particular, there is an intensive literature named "Benchmark on the Aerodynamics of a Rectangular 5:1 Cylinder" (BARC), is of great interest in the Civil Engineering due to of its similarity with the cross-section of skyscrapers (Fig. 1.1). In aerodynamics, this type of section is called *bluff body*. The study of bluff body wakes is important for applications in

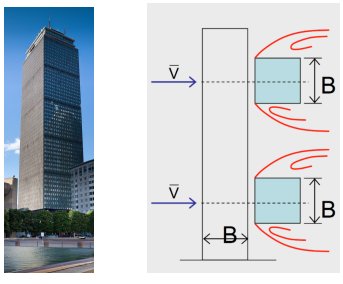


(a) (b)

Figure 1.1: Skyscraper cross-section

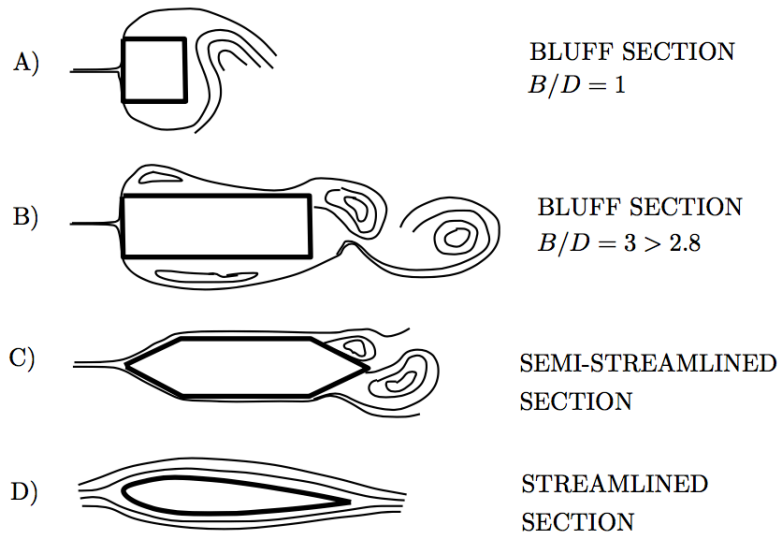


Figure 1.2: Aerodynamic classification of sections

aerodynamics, wind engineering, and electronics cooling. Bluff body cross sections that are often analyzed in the literature are circular and rectangular, and, overall, square. The flow features depend on Reynolds number and free stream turbulence. In particular, for square/rectangular cross section geometries, the orientation respect to the mean flow is another important parameter. In addition, the separation points are fixed for the square cylinder and they are depending on the Reynolds number. Moreover, the reattachment of the flow relies on the value of the ratio between the length and the height of the section, $B/D$, Fig. 1.2. On the opposite of the *bluff body*, the *streamlined* section has the boundary layer totally attached, so that the flux is laminar and the aerodymanics forces are steady. For example, the viscous effect is the principal contribution to the drag forcesd. The *semi-streamlined* section is a mix of the two previous sections.

Moreover, the square cylinder has a characteristic flow topology, as it is shown in the figure 1.3. In the present figure, we can differentiate three main regions: *Frontal region*, where the *stagnation point* is present in this zone. At this point, there is not velocity in the flow. In addition, across the frontal wall, the flow is affected by the viscous and turbulent stresses. In *Lateral region* the instability is generated. In fact, it is where the transition from laminar to turbulent regime take place. In addition, the flow becomes rotational and a reattatchment point could appear. Finally, in the *Base region*, the flow is moved by convective effectes and the vortical wake is located in this zone.

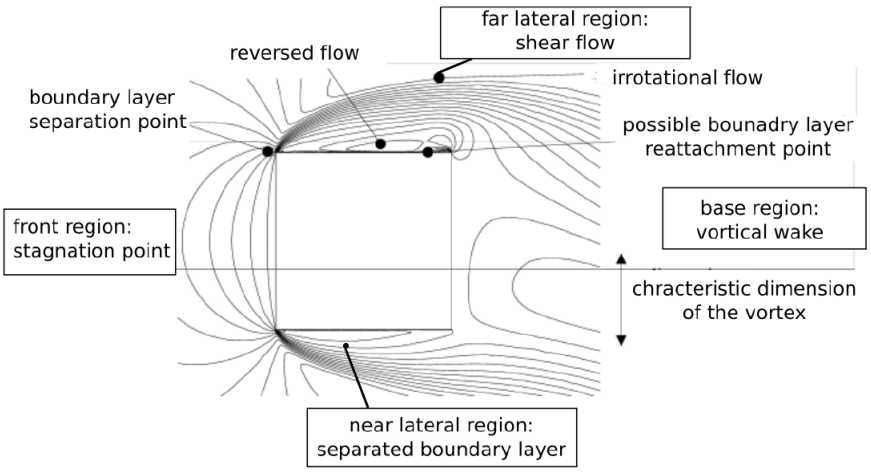


Figure 1.3: Flow topology using horizontal velocity contours

In order to quantify the complete effects of the flow in the structures, it is useful to calculate the time-averaged and maximum values of the aerodynamic coefficients, i.e. drag and lift. In addition, computing vorticity and streamlines could help to reveal some feature of the flux, as well as the velocity profiles.

Finally, an overview of the literature is useful to comprehend the theoretical concepts and to compare our results, so that we can have an idea about the influences of quality grids.

# Chapter 2

# Literature Review: Benchmark computations for flows around a stationary cylinder

In the literature, the study of the flow around a square or circular cylinder has strongly been analysed and developed. In this chapter, we will present a general overview of studies about cylinder simulations, so that the essential aspects of this subject and the correct construction of the model can suggest us how to determine accurate solution close to the bibliography.

## 2.1 General problem

A typical problem for cylinder is shown in Fig. 2.1 from *Rosetti and Vaz* [9], where a rectangular domain is used for the simulation of the flow. It presents the boundary conditions. It is confirmed that "it is appropriate to set the inlet and lateral boundaries $10D$ away from the cylinder axis whereas the outlet boundary can be located $20D$ away from the cylinder"[9]. The boundary conditions generally applied in this kind of problems are the Non-slip condition on the wall boundary, a periodic condition on the lateral regions and a inlet and outlet boundary conditions.

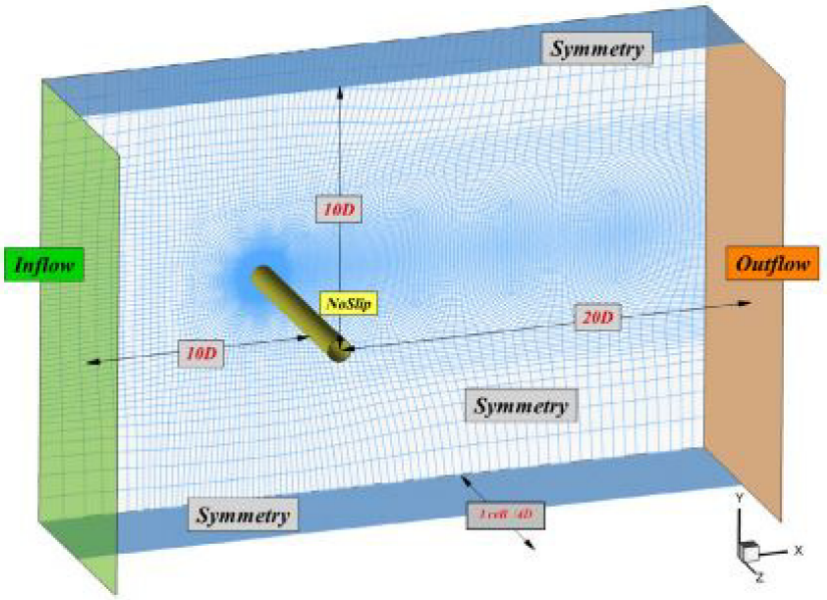


Figure 2.1: General grid and domain.

In order to solve these problems, an efficient mesh needs to be defined. It is well known that the quality of grid has a great influence on the numerical solutions. Several studies have shown that high quality structured grids can be generated easily to study the flows around a stationary cylinder. For example, in *Ye and Wan* [8], a general type of mesh is shown. In Fig.2.2 it can be noticed the grid layout and the size of the computational domain, in which $N$ is the number of grid nodes. Three grid components are used, which are a block around the cylinder, a transition block and a background block. The transition and background blocks are completely orthogonal. In order to have accurate solutions of the flow near the cylinder and in the wake, the block around the cylinder and the transition block are refined. The background block is coarsened, so that the amount of grid cells are not much higher and the computational cost is decreased. In this Thesis, a similar layout will be constructed.

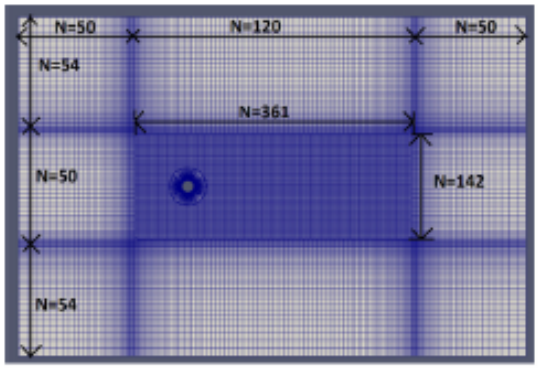


(a) Global layout

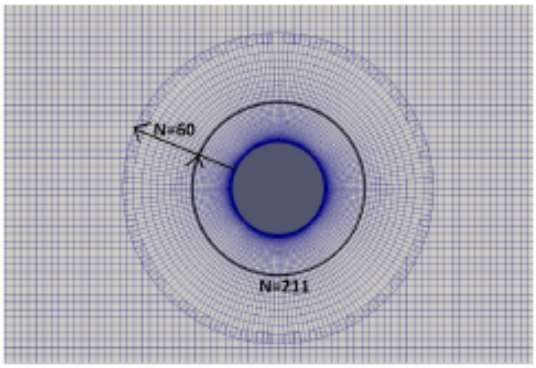


(b) Layout near the cylider

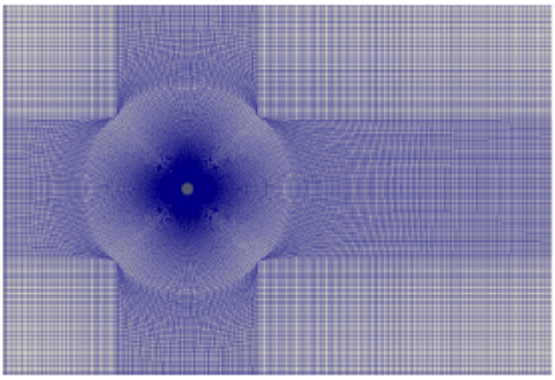

(c) Layout without overset

Figure 2.2: Layout grid

However, although in *Ye and Wan* [8] we can see a general problem with a general grid layout, their study is not focused on a grid investigation and they work on a circular cylinder. Then, in *Hu, Tse, Kwok and Zhang* [13], we can see a study about a cylinder nested in a square prism. A hybrid grid style was adopted. The main feature of the grid scheme is that the grid near the cylinder is fine enough while it is coarser in the far field. In addition, the grid is unstructured inside the square prism whereas structured outside the prism. In Fig.2.3 it is shown the mesh for the whole computational domain. As we can see in Fig. 2.3(c), there is a viscous boundary layer with 20 grid layers next to the

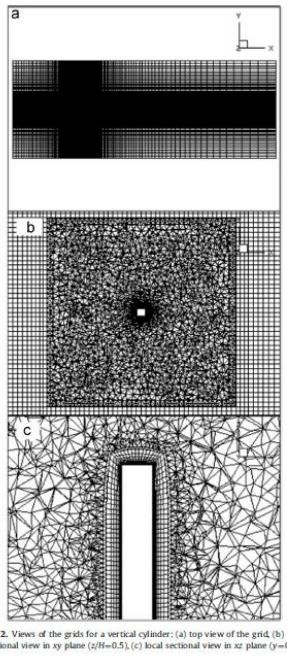


Fig. 2. Views of the grids for a vertical cylinder: (a) top view of the grid, (b) local sectional view in xy plane (z/H=0.5), (c) local sectional view in xz plane (y=0).

Figure 2.3: Views of the grids for a vertical cylinder: (a) top view of the grid, (b) local sectional in xy plane, (c) local sectional view in xz plane

surfaces of the cylinder. However, this study is about inclination angle on the cylinder. In the next section, we will see several studies about comparison between different grids.

## 2.2 Previous grid study

### 2.2.1 Grid comparison

In this section, we will see several previous studies about different meshes. Firstly, a Large-Eddy Simulation, LES, model applied to a structured or unstructured mesh is described in *Cao and Tamura* [15]. The model is a flow with $Re = 2.2 \cdot 10^4$ on a square culinder. The computational domain size is 28D x 24D x 4D. As shown the Fig.2.4(c), the corners of the square cylinder are rounded with $D/100$ radius of curvature. Aerodynamic features are not so much affected by these corners.
In this article, between the objectives, meshing strategies and effects of spanwise resolution and length are investigated. So, several computational meshes have been set up to be studied in order to improve the accuracy. Firstly, a structured grid refined near the cylinder is named CR, while WR and CWR have hybrid grids where, respectively, are wake refined and wake and cylinder refined. Finally, the CWR has been selected as the optimal mesh. Furthermore, using meshing strategy of CWR, effects of spanwise resolution and length is investigated. Two cases are evalutated: CWR2k, in which the spanwise resolution is twice refined and CWR14D, where the spanwise length is increased to 14D. Moreover, CWR is $30 - 50\%$ cheaper than CR, while CWR2k and CWR14D are 2.5 and 4.4 times as expensive as CWR. After all of this, comparison of interest quanti-

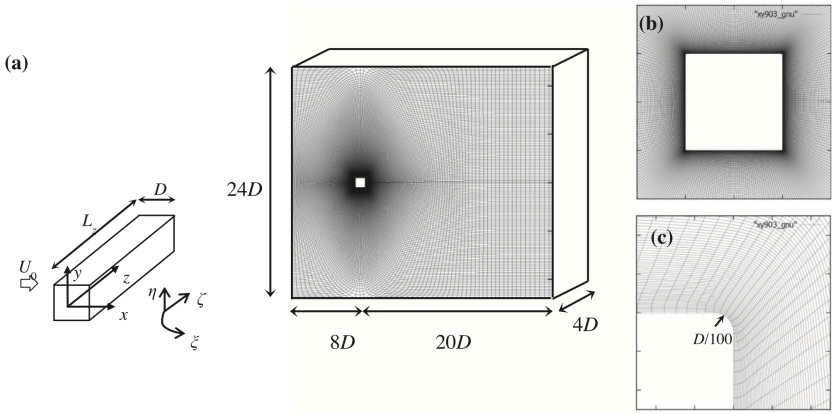


Figure 2.4: Computational domain size in a generalized coordinates. (a) Total grid system; (b) Near the square cylinder; (c) Near the corner of the square cylinder with its radius of curvature

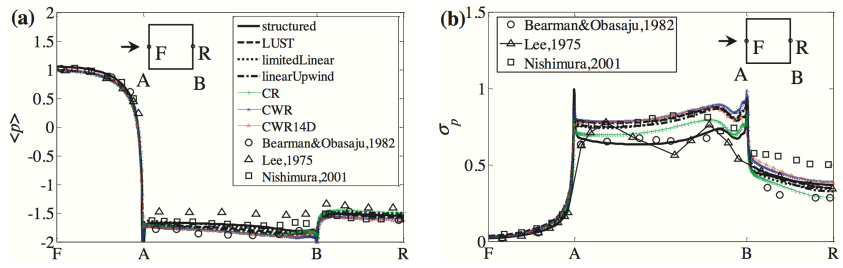


Figure 2.5: Distribution of pressure on the cylinder surface: (a) time-averaged pressure; (b) fluctuating pressure

ties are shown. We can see in following figures (2.5-2.6-2.7-2.8) comparison of pressure distribution, of wake flow, of shear layer flow, where in particularly we see profiles of velocity along the vertical direction, $x/D = -0.25$, $x/D = 0$, $x/D = 0.25$ and $x/D = 0.5$. $x/D = 0$ is the vertical line that intersects the cylinder in two equal parts. Even in this Thesis, we will see a comparation of velocity profiles in this way. Moreover, even comparison about lift and drag coefficient are shown. All of this quantities will be analyzed even in this Thesis. In fact, we can see from graphics substantial differences between the several grids. However, a study between orthogonal and non-orthogonal meshes is not present in this study. Of consequence, it is necessary to make a systematic study about grids, to see better the differences on the result between different types of mesh: structured or unstructured, orthogonal or non-orthogonal, etc.

### 2.2.2 Grid quality index

In *Kallinderis and Kontzialis* [10], we can see an application of a grid quality index on mesh construction. It is based on a priori evaluation of the shape and topology of grid. This measure has several properties as the simple mathematical form and accuracy to capture distortions in any direction. It has a direct relations with the truncation error

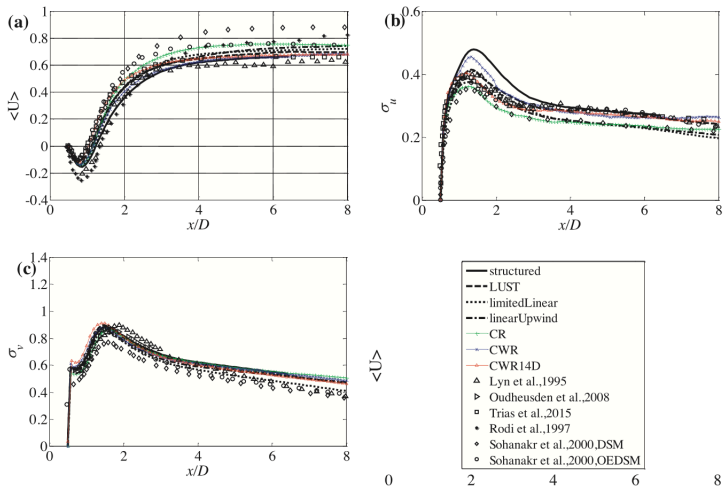


Figure 2.6: (a) Time-averaged stream-wise velocity; (b) Fluctuation of stream-wise velocity; (c) Fluctuation of the vertical velocity

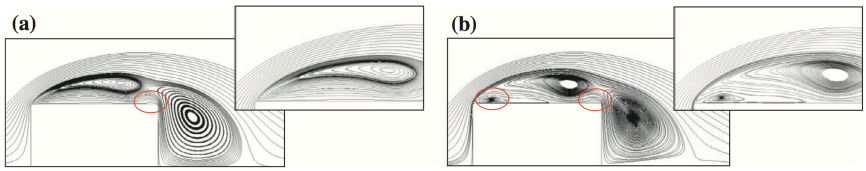


Figure 2.7: Streamlines of time-averaged velocity in the cases: (a) Structured; (b) CWR

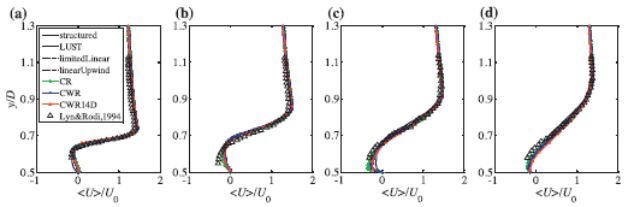


Figure 2.8: Velocity profiles along the vertical direction in the shear-layer region. (e) Time-averaged stream-wise velocity when $x/D = -0.25$, $x/D = 0$, $x/D = 0.25$, $x/D = 0.5$

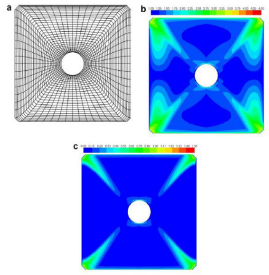

Figure 2.10: Structured mesh around a cylinder: (a) mesh geometry, (b) index $q$ and (c) index $Q$

and can detect relatively small distortions where there are larger ones. Finally, the index have to be independent of the local size of the grid.

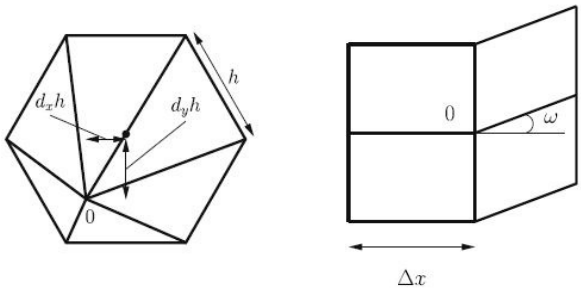


(a) (b)

Figure 2.9: In (a) stretching for unstructured mesh, in (b) skewed mesh

In this study, we have two mesh quality index $Q_x$: for (1) the *stretched unstructured* mesh (Fig.2.9(a)) and for (2) the *skewed* mesh (Fig.2.9(b)). There is another index $q$ that uses both the first and the second order terms, while index $Q$ only first order. Both indices are evaluated in cylinder mesh, that has mild distortion away from the body surface. Then it is convenient at the farfield to check the performance of the quality indices. As we can see in Fig. 2.10, skewness is shown along lines off the surface that are diagonal. Both indices suggest that we have a good grid quality close to the cylinder. However, the index $Q$ capture better the fou skewness lines than the other index. On the other hand, for the hybrid grid shown in Fig.2.11, between the quadrilaterals and the triangles, where we have strong distortions in the farfields, it can be noticed irregularity of the interface. So, both types of distortions are well recognized by these indices. In

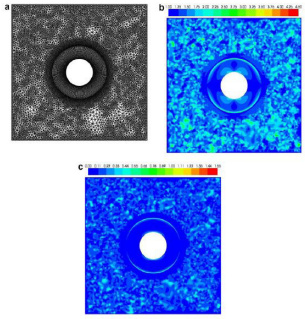

Figure 2.11: Hybrid mesh around a cylinder: (a) mesh geometry, (b) index $q$ and (c) index $Q$.

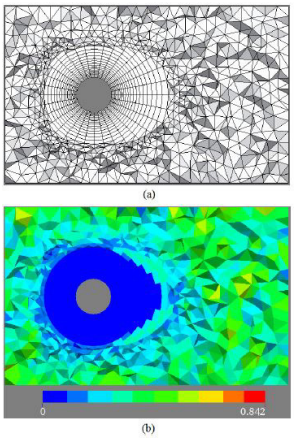


Figure 2.12: 3-D cylinder: (a) Hybrid grid fieldcut, and (b) the corresponding distribution of the mesh quality index ($Q$)

conclusion, index $Q$ is recommended because of its simple calculation. A disadvantage of $Q$ is that has not second order accurate computation of the gradient, so that can not capture the related quality of distorted grids.

Another work using quality index is from *Fotia and Kallinderis* [11]. In this study we can see in Fig.2.12, an application of the mesh quality index in a hybrid mesh around a 3-D cylinder. At the boundary layer, the quality index is close to zero, i.e. have its optimal value, beacuse it is composed by uniform hexahedra. It can be noticed in the interface and in the farfield an increase of index $Q$, that indicates a poor grid quality.

In conclusion, all of this works we suggest how to construct a mesh on a square cylinder. The grid quality error is partially examined, but an exhaustive literature in CFD and CWE applications are not still present. The aim of this Thesis is to show a computational and systematic study between several grids which present grid quality errors. So, in the following chapters it is shown CFD methodology and a theoric explanation about grid quality error in general. Finally, in the last chapters, the study will be explained and the results will be discussed, verifying the effects of the mesh quality.

### 2.2.3 Grid quality studies

An important study of *Ichiro Nakane* [21] proves the validity of grid orthogonality on two-dimensional calculation for the flow around a circular cylinder. Five kinds of calculation grids (one non-orthogonal and four orthogonal grids) are generated. However, *Nakane* used body fitted curvilinear coordinate systems ("BFC") method to generate the mesh. Usually the coordinate lines of this BFC grid are non-orthogonal. Of consequence, there is a possibility that the calculation accuracy with non-orthogonal body-fitted curvilinear coordinate systems ("NBFC"), as we can see in Fig.2.13, is low compared to orthogonal ones ("OBFC").

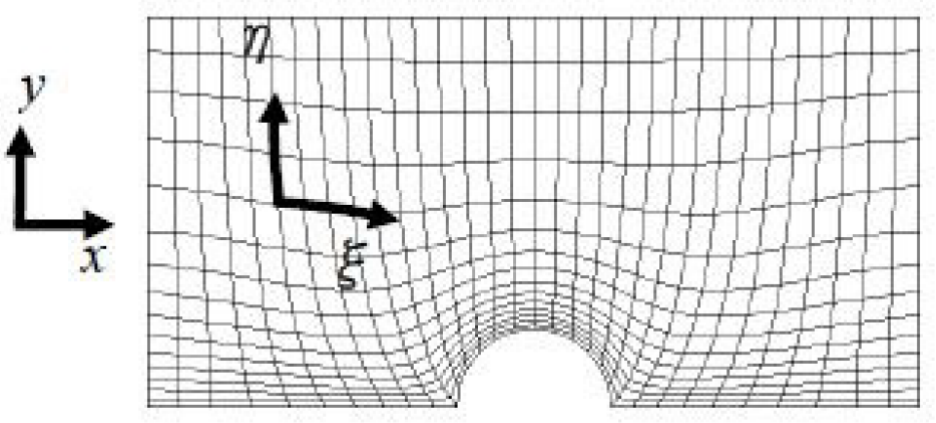


Figure 2.13: Scheme of NBFC grid

So, the four kinds of OBFC grids around a circular cylinder are generated from a NBFC grid by an integral method, where the orthogonal regions from the cylindrical wall are different as follows: first 5-lines ($\xi_0 = 5$), 15-lines ($\xi_0 = 15$), 25-lines ($\xi_0 = 25$) and 35-lines ($\xi_0 = 35$).

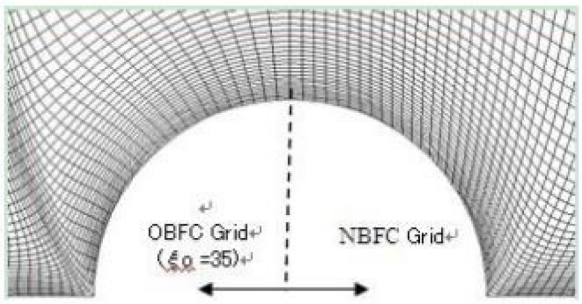


Figure 2.14: Comparison between OBFC Grid $\xi_0 = 35$, (left) and NBFC grid (right).

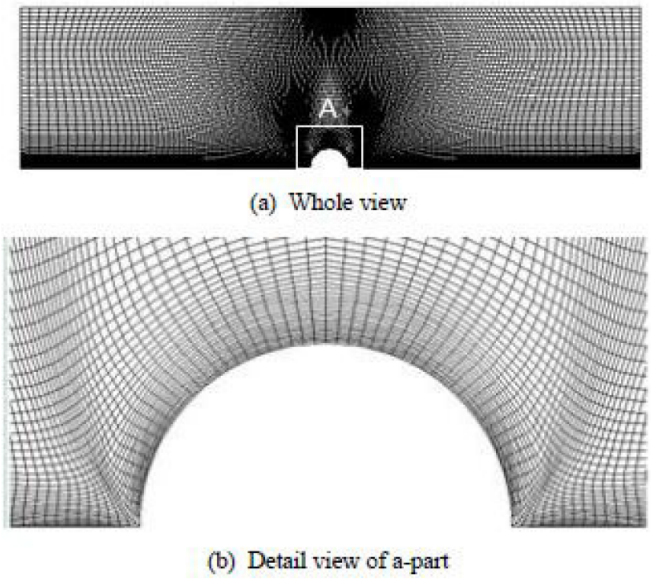


Figure 2.15: (OBFC grid $\xi_0 = 15$)

The OBFC grids generated using this method is shown in Fig.2.14 and Fig.2.15 In particular, Fig.2.14 shows the comparison of the original NBFC grid and the OBFC ($\xi_0 = 35$), in which we can see each quarter circle cut out and connected. In addition, from Fig.2.15 it can also be verified that the coordinate lines for the coordinate lines for the orthogonal region and the non-orthogonal region join up smoothly. Moreover, coordinate lines are generated without changing these ones along the flow direction and the boundary point positions. By this means, the effectiveness of the orthogonal grid could be investigated. The results shown from this study indicate that the calculation results agree better with the visualization and the analysis for a wider orthogonal region in the coordinate system. It is confirmed in Fig.2.16, where the calculated wall pressure coefficient $C_p$ is compared with the analysis result of Collins and Dennis. The result calculated by the NBFC grid has larger difference with the analysis of Dennis, and the result by the $\xi_0 = 35$ OBFC grid has smaller difference with it. In other words, it is verified that the orthogonal grid is important in the numerical simulation and the proposed straightforward orthogonal grid generation method is sufficiently effective. Finally, it is demonstrated, as we can see in Fig.2.17 that the effect of this orthogonal grid is greater with Reynolds number $Re$ larger.

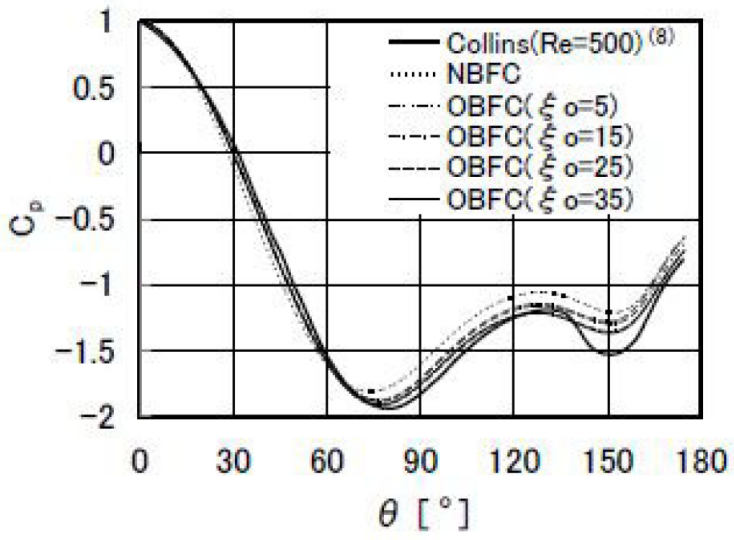


Figure 2.16: Wall pressure coefficient calculated by the orthogonal and non-orthogonal grids ($Re = 550$,$t^* = 1.4$)

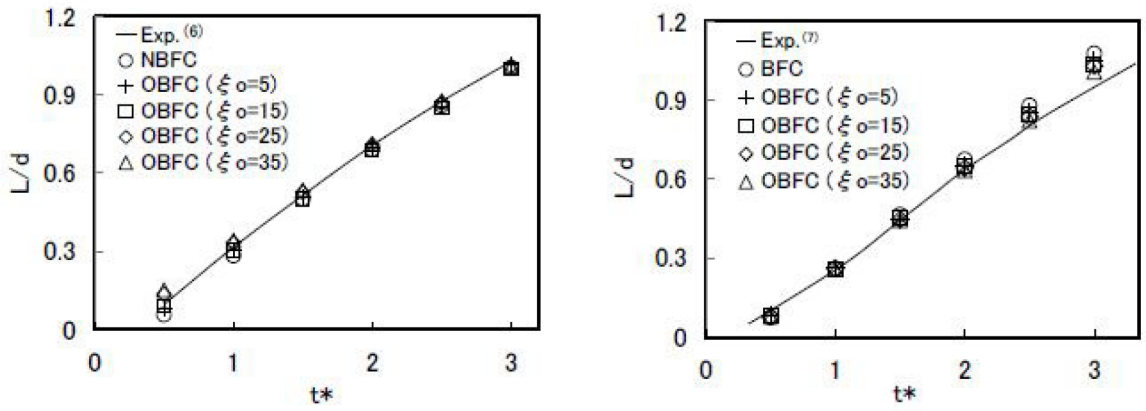


(a) $Re = 31$ (b) $Re = 1200$

Figure 2.17: Wake length calculated by the orthogonal and non-orthogonal grids

When $Re$ is small, the merits of the orthogonal grid are not readily reflected in the calculated results. But usually, in CFD applications, $Re$ is very big. Although these value of $Re$ are too small in our applications, it is well known that the orthogonality of a mesh is very important on the effects of numerical solutions, and in this Thesis will prove this issue.

Moreover, another interesting study is about the correlation between a grid quality metric and the accuracy of the solution. This work is provided by *Fattah, Angland and Zhang* [14]. Finite Difference Method is used and it is explained the methodology to obtain the grid quality metric for a 1D case. From the wave equation in the generalized

coordinates,

$$\frac{\partial f}{\partial t} + U\frac{\partial f}{\partial \xi}\frac{\partial \xi}{\partial x} = 0 \tag{2.1}$$

where $f$ is a scalar variable, $t$ is time, $U$ the convection speed in x-direction and $\xi$ the generalized coordinate, several numerical errors are generated. In particular, the term $\frac{\partial \xi}{\partial x}$ is known as the *metric of the grid transformation*. If the function $\xi$ is not well resolved along the x-coordinate, the truncation error will be greater. So, a mesh refinement should be done in order to reduce it, but it is not necessary to know a posteriori the results of the function $f$. In this article, the main reason of truncation error the metrics of the grid transformations. So, the aim of this study will be to define a *grid quality metric* related to the truncation errors of $\frac{\partial \xi}{\partial x}$.

In addition, the grid quality metric is generated with the objective of identifying the regions of the grid where the truncation errors are more important.

So, the grid quality metric, $Q$, is defined in 3D case as

$$Q = \sqrt{\left(\frac{\hat{\Delta}\xi}{\Delta\xi}\right)^2 + \left(\frac{\hat{\Delta}\eta}{\Delta\eta}\right)^2 + \left(\frac{\hat{\Delta}\zeta}{\Delta\zeta}\right)^2} \tag{2.2}$$

where

$$\hat{\Delta}\xi = \sqrt{\hat{\Delta}x_i^2 + \hat{\Delta}y_i^2 + \hat{\Delta}z_i^2} \tag{2.3}$$

and

$$\Delta\xi = \sqrt{x_\xi^2 + y_\xi^2 + z_\xi^2} \tag{2.4}$$

is defined to normalize the quantity of 2.3. If values of $Q$ is larger, it will mean that the value of the truncation error is greater, so that the grid has less quality. The grid quality metric can be computed for all grid points.

Then, with the numerical and analytical solutions, it can be computed the grid quality metric integrating values for the whole domain.

$$E = \frac{(\rho - \rho_{exact}}{\rho_{exact}} \tag{2.5}$$

$$Q_I = \int\int_S Q dx dy \tag{2.6}$$

$$E_I = \int\int_S |E| dx dy \tag{2.7}$$

So, now the problem is to solve for an uniform and other different grids in order to determine a correlation between the grid quality metric and inaccurate solutions.

- Uniform Grid:

  This is the ideal case that it will be used as reference to compute the solution error. In fact, the integrated values of the grid quality metric and the solution error are, respectively, $Q_I = O(10^{-9})$ and $E_I = O(10^{-5})$. Then, the truncation error for this grid is very small, so that we can consider this grid as a reference for the following meshes.

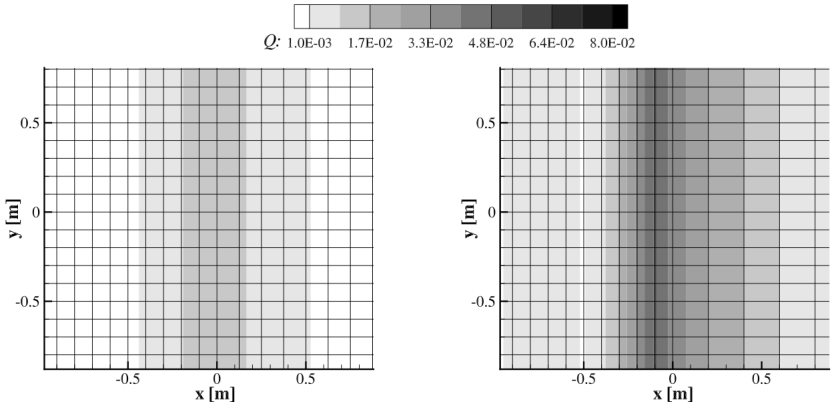


Figure 2.18: The effect on the grid quality metric when the grid spacing is modified at $x = 0$. $A_x = 1.25$ (left), $A_x = 2$ (right).

- Abrupt changes in the grid spacing:

  Applying the following expression to the grid coordinates of the uniform grid,

  $$x^*(\xi, \eta) = x(\xi, \eta) A_x H(x) \tag{2.8}$$

  an *abrupt change in the grid spacing* is obtained. $H(x)$ is the Heaviside function and $A_x$ is a constant related to the grid spacing size.

  From the Fig.2.18, it can be noticed that if the amount grid spacing size is higher, the grid quality metric $Q$ increases, so that it is obtained a poor grid quality.

- Abrupt change in the grid line direction:

  Insted, this following function imposed to the uniform grid leads to an *abrupt change in the grid direction.*

  $$y^*(\xi, \eta) = y(\xi, \eta) + H(x) A_y x(\xi, \eta) \tag{2.9}$$

  The grid line gradient is dependent from the constant $A_y$.

  As we can see in Fig.2.19, the solution accuracy is reduced if $A_y$ has greater value. In fact, the amount term $Q$ is higher.

- Uniformly skewed grids:

  To get an *uniformly skewed grid*, the following function is provided.

  $$x^*(\xi, \eta) = x(\xi, \eta) + A_s y(\xi, \eta) \tag{2.10}$$

  The grid line gradient across the entire domain is described by the term $A_S$. In the Fig.2.20, the skew angle does not influence the error.

- Non-uniformly skewed grids:

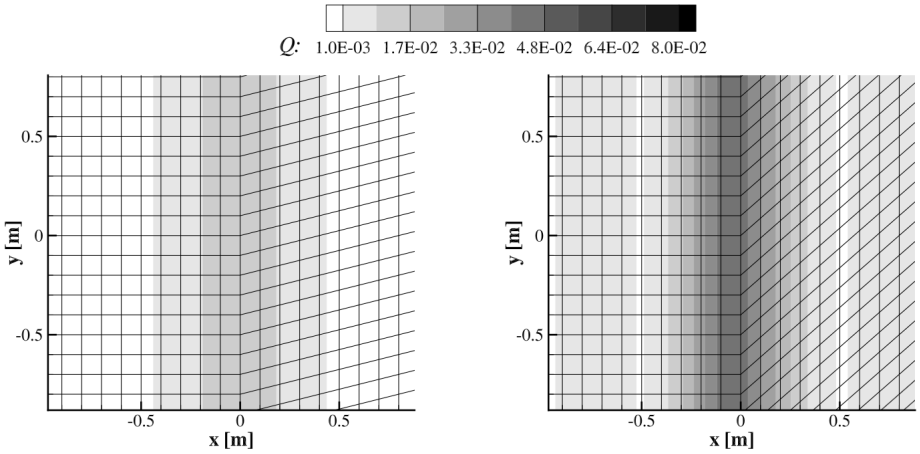


Figure 2.19: The effect on the grid quality metric when the grid line direction is modified at $x = 0$. $A_y = 0.25$ (left), $A_y = 0.875$ (right)

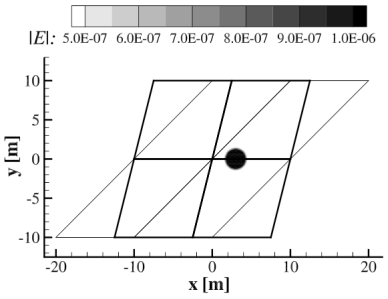


Figure 2.20: The effect on the solution error when the uniform cell skew is modified at $x = 0$. $A_s = 0.25$ (thick line), $A_s = 1$ (thin line)

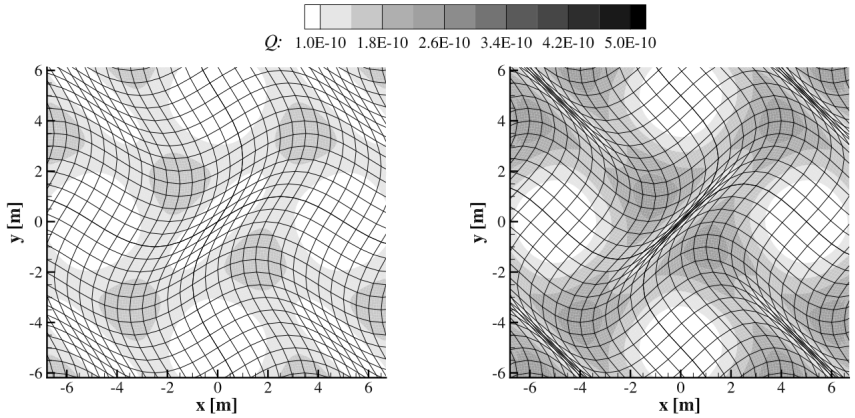


Figure 2.21: The effect on the grid quality metric when the $A_t$ is changed at $x = 0$. $A_t = 1$ (left), $A_t = 1.5$ (right)

Applying trigonometric functions, we will obtain a *non-uniformly skewed grid*.

$$x^*(\xi,\eta) = x(\xi,\eta) + A_t sin\Big(\frac{2\pi y(\xi,\eta)}{L}\Big) y^*(\xi,\eta) = y(\xi,\eta) + A_t sin\Big(\frac{2\pi x(\xi,\eta)}{L}\Big) \quad (2.11)$$

where $A_t$ is the amplitude and it is changing, while $L$ is the wavelength set to $L = 10m$.

From the Fig.2.21 we can see that the largest value of the grid quality metric $Q$ is located where the variations on the grid direction are higher. So, the quality of the grid is lowest.

- Grid stretching:

  In order to increase the grid resolution to a specific region, *grid stretching* is typically used. In this case, the y-direction is constant ($\Delta y = 0.1$), while the following transformations define the stream-wise spaces.

$$x^*(\xi) = A_h \tilde{x}(\xi) x^*(\xi) = A_h \Big[1 + \frac{\xi - \max(\xi)}{\xi_{BL} - 1}(\tilde{x}(\xi_{BL} - \tilde{x}(\xi_{BL} - 1))\Big] \quad (2.12)$$

  $A_h$ indicates the amount of stretching in the range $0 \leq x \leq A_h$. Outside this region, the stream-grid spacing is uniform. Then, the number f points in the stretched region is defind by $\xi_{BL}$. The equations above are implemented when $1 \leq \xi \leq \xi_{BL}$ and $\xi > \xi_{BL}$. $\tilde{x}$ is the normalized grid point distribution function. As we can see in the Fig.2.22, a lower grid quality metric and the consequent higher numerical errors are due to an amount of the grid stretching.

Finally, in order to demonstrate quantitatively a relation between the grid quality metric and the solution error, a correlation coefficient $C_{QE}$ can be defined as

$$C_{QE} = \frac{< Q_I E_I >}{[< Q_I^2 >< E_I^2 >]^{1/2}} \quad (2.13)$$

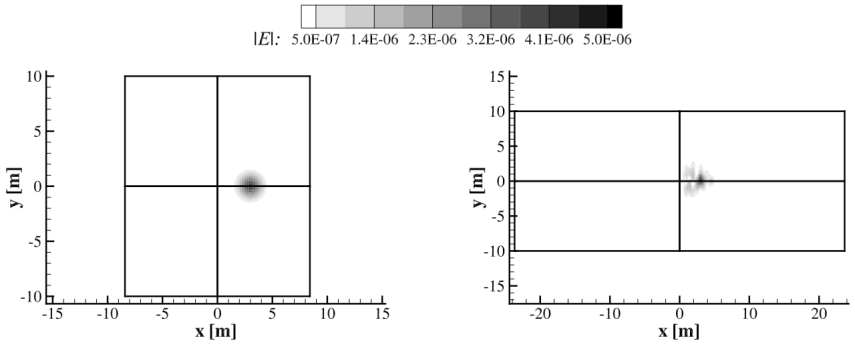


Figure 2.22: The effect on the solution accuracy when the grid stretching is changed at $x = 0$. $\alpha = 0.5$ (left), $\alpha = 3.5$ (right)

In the table 2.1, we have the results of correlation coefficients has been collected for each case of study. First of all, it can be seen that the uniform skewness grid does not affect the results.. On the other hand, a higher correlation coefficient are collected in the other cases with values over 0.9. So, a strong correlation is provided for these grids.

| Grid Features | Explicit filter | Implicit filters |
|---|---|---|
| Grid spacing discontinuity | 0.971 | 0.970 |
| Grid direction discontinuity | 0.955 | 0.954 |
| Uniform skewness | 0.427 | 0.128 |
| Non-uniform skewness | 0.921 | 0.921 |
| Grid stretching | 0.932 | 0.913 |

Table 2.1: Correlation coefficient for each case

In conclusion, *Nakane* [21] has confirmed the great influence that a non-orthogonal mesh on results. However, his study is different from what we aim to search. First, we will study a square cylinder, not circular. Then, we will analyze other important quantities used in CFD and CWE applications like lift and drag coefficients, etc. So, his work has suggested ulterior motivation to elaborate this argument of research. Last, but not least, *Fattah, Angland and Zhang* [14] have provided a strong correlation between grid quality metric and the solution error. Even in this Thesis, although in a different way, we will compute a correlation coefficient between a grid quality measure and solution errors.

# Chapter 3

# Numerical methods in CWE: Introduction

*Computational Wind Engineering*, *CWE*, is the application of *Computational Fluid Dynamics*, *CFD*, in wind engineering. In this field, the kind of problem of this Thesis, is of great interest, specially in the field of structural engineering, due to it is very important to obtain accurate results.

There are many codes, but we are going to use *ANSYS: Fluent/CFX* software to complete this Thesis. In general, in CWE simulations, the basic scheme could be defined as:

1. Turbulent flux models
2. Discretization models of the equations
3. Computation grid generation

These issues are often in relation in their formulation, are closely dependent in calculation model definition and their effects are difficult to distinguish. In this chapter we analyze the first two issues. Computation grid generation will be discuss in the next chapter.

## 3.1 Turbulent flux models

### 3.1.1 The governing equations

In *Fluid Dynamics*, we approximate the fluid as a *continuum*. It implies that even an infinitesimally small element of the fluid still contains a sufficient number of particles, so that we mean velocity and mean kinetic energy can be defined. In addition, velocity, pressure, temperature, density and other important quantities at each point of the fluid can be computed.

Defining a *finite control volume*, a certain flow quantity is transported across the boundary. The amount of the quantity crossing the boundary is called *flux*. The flux can be in general decomposed into two different parts: one due to the *convective* transport and the other one due to the *diffusive* nature, that it is dependent to the gradient of the quantity considered.

The derivation of the principal equations of fluid dynamics is based on the fact that the dynamical behaviour of a fluid is determined by the following *conservation laws*, namely:

1. *The conservation of mass*: the *Continuity Equation* is derived from this law. The mass can not be created in such a fluid system and can not disappear from it. Since for a fluid at rest, any variation of mass would imply a displacement of fluid particles, in the continuity equations no diffusive flux takes part. In order to derive the continuity equation, considering a finite control volume fixed in space, we have the integral conservative form of this equation equation:

$$\frac{\partial}{\partial t}\int_V \rho dV + \oint_{\partial V} \rho(\bar{v}\cdot\bar{n})dS = 0 \tag{3.1}$$

   Using Gauss theorem, we obtain differential form of the 3.1:

$$\frac{\partial \rho}{\partial t} + \nabla\cdot(\rho\bar{v}) = 0 \tag{3.2}$$

2. *The conservation of momentum*: the *Momentum Equation* is build recalling the Newton's law, i.e. the variation of momentum is caused by the net force acting on an mass element. So, we obtain the integral form,

$$\frac{\partial}{\partial t}\int_V \rho\bar{v}dV + \oint_{\partial V}\rho\bar{v}(\bar{v}\cdot\bar{n})dS + \oint_{\partial V}\rho\bar{n}dS - \oint_{\partial V}(\bar{\bar{\tau}}\cdot\bar{n})dS = \int_V \rho\bar{f}_e dV \tag{3.3}$$

   where $\bar{\bar{\tau}}$ is *viscous stress tensor*, proportional to the velocity gradient. The differential form of the 3.3 is:

$$\frac{\partial \rho\bar{v}}{\partial t} + \nabla\cdot(\rho\bar{v}\bar{v}) + \nabla p - \nabla\cdot\bar{\bar{\tau}} = \rho f \tag{3.4}$$

3. *The conservation of energy*: from the First Law of Thermodynamics, the *Energy Equation* is derived. Applied to the control volume, the total energy per unit mass $E$ of a fluid is composed by internal energy per unit mass $e$ and kinetic energy $|\bar{v}|^2/2$. Then, the total energy is written as $E = e + \frac{|\bar{v}|^2}{2}$. The integral conservative form is

$$\frac{\partial}{\partial t}\int_V \rho E dV + \oint_{\partial V}\rho E(\bar{v}\cdot\bar{n})dS = \oint_{\partial V} k(\nabla T\cdot\bar{n})dS + \int_V(\rho\bar{f}_e\cdot\bar{v}+\dot{q}_k)dV - \oint_{\partial V} p(\bar{v}\cdot\bar{n}dS) + \oint_{\partial V}(\bar{\bar{\tau}}\cdot\bar{v})\cdot\bar{n}dS \tag{3.5}$$

   The differential conservative form of the balance equation is

$$\frac{\partial}{\partial t}\rho E + \nabla\cdot\rho E\bar{v} = \nabla\cdot k(\nabla T + \rho\bar{f}_e\cdot\bar{v} + \dot{q}_h - \nabla\cdot p\bar{v} + \nabla\cdot(\bar{\bar{\tau}}\cdot\bar{v}) \tag{3.6}$$

   The Navier-Stokes equations represent in three dimensions a system of five equations for the five conservative variables,$\rho$,$\rho u$,$\rho v$,$\rho w$,$\rho e$. But they contain seven unknown flow field variables, $\rho$,$u$,$v$,$w$,$e$,$p$, and $T$. Then, two additional equations are needed. We can impose thermodynamic relations between the states variable, like the internal energy as a function of pressure and temperature $e = f(p,T)$. In general, a fluid can be considered as a *perfect gas*, so that the equation of state takes the form $p = \rho RT$, where $R$ is the specific gas constant. Now we have all the equations to compute all the variables.

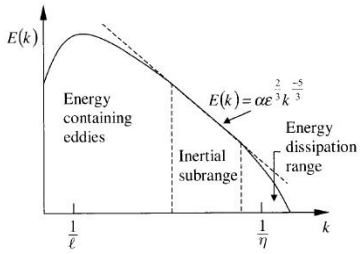


Figure 3.1: Energy spectrum vs. wave number space (log-log scales)

### 3.1.2 Turbulence modelling

Turbulence is a natural phenomenon in fluids that occurs when velocity gradients are high, in particular when high Mach numbers and high Reynolds numbers are characteristics of a flow. In addition, turbulent flows grows in contact with walls or in between two neighboring layers. Due to velocity gradients increasing, the flow becomes rotational, leading to a vigorous stretching of vortex lines, which cannot be supported in two dimensions. Then, turbulent flows are physically three-dimensional, typical of random fluctuations.
In turbulent flows, large and small scales of continuous energy spectrum are merged. There are defined eddies, i.e. different vortex structures, that are overlapping in space, with large ones carrying small ones. Beacuse of the presence of different scales in the flow, turbulent Reynolds numbers can be defined as

$$Re_\lambda = \frac{\lambda v_\lambda}{\nu} \tag{3.7}$$

where $\lambda$ is the dimension of the spatial scale. If $\lambda$ is large, the amount of $Re_\lambda$ leads to an insignificant viscous diffusion. On the other hand, the viscosity is more important at the smallest scales, $Re_\lambda \sim 1$. These scales are known as *Kolmogorov scales* and the spatial dimension is represented with $\eta$. The energy is transported from largest to smallest scales by the intermediate scales, better known as *inertial scales*. Then, from larger to smaller eddies the kinetic energy is transfered, and the dissipation into heat occurs in the smallest eddies. This phenomena is called *Turbulent energy cascade*, In the fig.3.1 we can see this process.

The computation of turbulent flows is much difficult beacuse of the time scales have a big range of length. All this even if the flow variables are of deterministic nature. So, several numerical methods are provided to compute these types of flows.

1. Direct Numerical Simulation, DNS

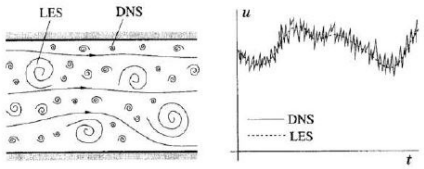


Figure 3.2: Comparison between LES and DNS methods

In *Direct Numerical Simulation*, all the turbulence scales, even the Kolmogrov microscale, are computed, so that we can totally resolve the Navier-Stokes system of equations. However, we need a very refined mesh with high computational cost. To have an idea, starting with

$$\eta = (\nu^3/\varepsilon)^{1/4} \tag{3.8}$$

, we know that the turbulence scales have values from the large energy-containing eddies to the dissipation scales, i.e. $0.1 \leq k\eta \leq 1$, where $k$, wave number, is computed. So, the number of grid points $N$ required for a mesh is proportional to $L/\eta \approx Re^{3/4}$, where $L$ is the characteristic length. Finally, this leads to the number of grid points in 3-D proportional to

$$N = Re^{9/4} \tag{3.9}$$

and the CPU-time as $Re^3$. Of consequence, although the results are very accurate, DNS is only used in simple geometries and low Reynolds numbers.

2. Reynolds-Averaged Navier-Stokes, RANS
In this method, every variable $\phi$ can be approximated statistically with a mean component $\bar{\phi}$ and a fluctuating component $\phi'$:

$$\phi(x_i, t) = \bar{\phi}(x_i, y) + \phi'(x_i, t) \tag{3.10}$$

where the mean component in an unsteady flow can be written as

$$\bar{\phi(x_i}, t) = \lim_{N\to\infty} \frac{1}{N} \sum_{n=1}^{N} \phi(x_i, t) \tag{3.11}$$

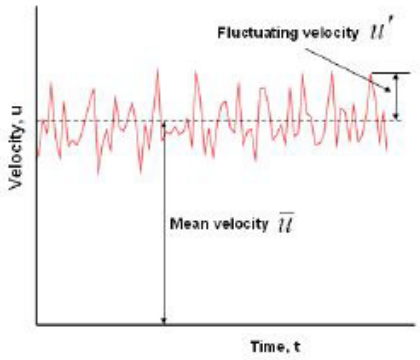


Figure 3.3: Instantaneous and average velocity in turbulent velocity

where $N$ is the number of members in the sum great as well as the effect of the fluctuations are eliminated. Then, we obtain the *Reynolds-averaged Navier-Stokes equations*, that, written for incompressible flows, are

$$\frac{\partial(\rho\bar{u}_i)}{\partial t} + \frac{\partial}{\partial x_j}(\rho\bar{u}_i\bar{u}_j + \rho\bar{u_i'u_j'}) = -\frac{\partial\bar{p}}{\partial x_i} + \frac{\partial\bar{\tau}_{ij}}{\partial x_j} \tag{3.12}$$

where $R_{ij} = \bar{u_i'u_j'}$ is called *Reynolds-stress tensor*. Moreover, $\bar{u}_i\bar{u}_j$ is known as the *scalar flux* and $\bar{\tau}_{ij}$ are the mean viscous stress tensor components:

$$\bar{\tau}_{ij} = \mu\Big(\frac{\partial\bar{u}_i}{\partial x_j} + \frac{\partial\bar{u}_j}{\partial x_i}\Big) \tag{3.13}$$

However, if the Reynolds averaging is applied to the mass and energy balance equations, we obtain a system of equations which is not closed. Closure requires use of some approximations, which take from prescribing the Reunolds-stress tensor and the turbulent scalar flux. Examples of RANS model are the $K-\varepsilon$ STD and $K-\varepsilon$ RNG model.

In essence, turbulence can be characterized by its kinetic energy ($k$) or velocity ($q = \sqrt{2k}$) and a length scale ($L$). The turbulent kinetic energy is defined by the following expression:

$$k = \frac{1}{2}\overline{u_i'u_i'} = \frac{1}{2}(\overline{u_x'u_x'} + \overline{u_y'u_y'} + \overline{u_z'u_z'}) \tag{3.14}$$

Due to the complexity related to the description of the turbulence quantities suggests that one might use partial differential equations to compute them. The equation for the *turbulent kinetic energy*, $k$, is written as

$$\frac{\partial(\rho k)}{\partial t} + \frac{\partial(\rho \bar{u_j} k)}{\partial x_j} = \frac{\partial}{\partial x_j}\left(\mu \frac{\partial k}{\partial x_j}\right) - \frac{\partial}{\partial x_j}\left(\frac{\rho}{2}\overline{u_j' u_i' u_i'} + \overline{p' u_j'}\right) - \rho \overline{u_i' u_j'} \frac{\partial \bar{u_i}}{\partial x_j} - \mu \overline{\frac{\partial u_i'}{\partial x_k} \frac{\partial u_i'}{\partial x_k}} \tag{3.15}$$

The last term represents the product of the density ($\rho$) and the dissipation ($\epsilon$), when the turbulence energy is converted into internal energy. The second term on the right-hand side of the expression 3.15 is known as *turbulent diffusion*, which can be modeled like

$$-\left(\frac{\rho}{2}\overline{u_j' u_i' u_i'} + \overline{p' u_j'}\right) \approx \frac{\mu_t}{\sigma_k} \frac{\partial k}{\partial x_j} \tag{3.16}$$

where $\sigma_k$ is the turbulent Prandtl number and its value approaches unity.
The third term of the right-hand side represents the rate of production of turbulent kinetic energy by the mean flow. If we estimate the Reynolds stress using the eddy viscosity, the equation results

$$P_k = -\rho \overline{u_i' u_j'} \frac{\partial \overline{u}_i}{\partial x_j} \approx \mu_t \left(\frac{\partial \overline{u}_i}{\partial x_j} + \frac{\partial \overline{u}_j}{\partial x_i}\right) \frac{\partial \overline{u}_i}{\partial x_j}. \tag{3.17}$$

As mentioned above, two equations are required to close the set of equations. In turbulence, it is widely known that energy is tranferred from the largest scales to the smallest until it is dissipated. This relationship can be formulated.

$$\epsilon \approx \frac{k^{3/2}}{L} \tag{3.18}$$

So, the equation of the dissipation (3.19) allows us to complete the model.

$$\frac{\partial(\rho \epsilon)}{\partial t} + \frac{\partial(\rho u_j \epsilon)}{\partial x_j} = C_{\epsilon 1} P_k \frac{\epsilon}{k} - \rho C_{\epsilon 2} \frac{\epsilon^2}{k} + \frac{\partial}{\partial x_j}\left(\frac{\mu_t}{\sigma_\epsilon} \frac{\partial \epsilon}{\partial x_j}\right) \tag{3.19}$$

In this model, the eddy viscosity is defined like

$$\mu_t = \rho C_\mu \sqrt{k} L = \rho C_\mu \frac{k^2}{\epsilon} \tag{3.20}$$

The commonly values of the parameters are: $C_\mu = 0.09$, $C_{\epsilon 1} = 1.44$, $C_{\epsilon 2} = 1.92$, $\sigma_k = 1.0$ and $\sigma_{epsilon} = 1.3$.

To be exact, we use the *RNG* $k - \epsilon$ model, which is derived from the instantaneous Navier-Stokes equations, but applying a rigorous technique, known as *renormalization group theory*. It results similar to the $k - \epsilon$ equations explained before, but with different constants and additional terms. Also, non equilibrium wall functions are imposed as a condition near the wall.

3. Large Eddy Simulations, LES
   A compromise between DNS and RANS is the large eddy simulations. While large-scale eddies are exactly computed, small scales are modeled instead. So, the computational cost of a mesh much higher than in RANS, while, beacuse of the modeled small-scale turbulence, it is cheaper than DNS.
   The velocity field is filtered to have only the large scale components of the total field. Then, it is defined as

$$\bar{u_i}(x) = \int G(x, x')u_i(x')dx' \tag{3.21}$$

   where $G(x, x')$ is the filter kernel and it is a localized function.
   When the Navier-Stokes equations are filtered, one obtains:

$$\frac{\partial(\rho\bar{u_i})}{\partial t} + \frac{\partial(\rho u_i\bar{u}_j)}{\partial x_j} = -\frac{\partial\bar{p}}{\partial x_i} + \frac{\partial}{\partial x_j}\Big[\mu\Big(\frac{\partial\bar{u_j}}{\partial x_j} + \frac{\partial\bar{u_j}}{\partial x_i}\Big)\Big] \tag{3.22}$$

   However, $u_i\bar{u}_j \neq \bar{u}_i\bar{u}_j$. So, a modeling approximation of the difference between these quantities is needed to be introduced. Then, we define the *subgrid-scale Reynolds stress* as

$$\tau_{ij}^s = -\rho(u_i\bar{u}_j - \overline{\bar{i}\bar{j}}) \tag{3.23}$$

   . It can be interpretated as the phenomena related to the momentum flux that in the large scales is affected by the action of the small scales.

### 3.1.3 Boundary conditions

Despite of the numerical methodology chosen to solve the governing equations, we have to impose suitable *initial* and *boundary* conditions. The initial conditions determine the state of the fluid at the time $t = 0$. However, it is needed that the governing equations are satisfied by the initial condition.
Furthermore, the computational domain creates itself artificial boundaries. So, the physical quantities are needed to be defined. In order to avoid non-physical phenomena in the flow field. boundary conditions are applied in the *inlet*, *outlet* and *periodic boundary*.
Finally, there is a laste type of boundary condition. It is related to the interactions between the surface of a body and the fluid. It is imposed the *no slip* boundary condition $u = v = w = 0$ at the surface, that means no relative velocity between the surface and the fluid immediately at the surface is assumed.
Boundary condition affects not only the accuracy of the solution, but also the robustness and the convergence speed.

## 3.2 Discretization methods of the equations

The first step is the spatial discretization of the Navier-Stokes equations, which consists in the numerical approximation of the convective and the viscous fluxes, as well as of the source term. The spatial discretization schemes can be divided into the following three main categories: *finite difference*, *finite volume*, and *finite element*. All these methods rely on some kind of grid in order to discretize the governing equations.

### 3.2.1 Finite Difference Method

The basic idea of finite difference methods is simple: derivatives in differential equations are written in terms of discrete quantities of dependent and independent variables, resulting in simultaneous algebraic equations with all unknowns prescribed at discrete mesh points for the entire domain.
In Fluid Dynamics applications, in order to conform to the nature of the flows, different forms of the finite difference equations are written.
Consider a function $u(x)$ and its derivative at point $x$.

$$\frac{\partial u(x)}{\partial x} = \lim_{\Delta x \to 0} \frac{u(x + \Delta x) - u(x)}{\Delta x} \tag{3.24}$$

If $u(x + \Delta x)$ is expanded in Taylor series about $u(x)$, we obtain

$$u(x + \Delta x) = u(x) + \Delta x \frac{\partial u(x)}{\partial x} + \frac{(\Delta x)^2}{2} \frac{\partial^2 u(x)}{\partial x^2} + \frac{(\Delta x)^3}{3!} \frac{\partial^3 u(x)}{\partial x^3} + ... \tag{3.25}$$

So, we derive

$$\frac{u(x + \Delta x) - u(x)}{\Delta x} = \frac{\partial u(x)}{\partial x} + \frac{\Delta x}{2} \frac{\partial^2 u(x)}{\partial x^2} + ... = \frac{\partial u(x)}{\partial x} + O(\Delta x) \tag{3.26}$$

The derivative $\frac{\partial u(x)}{\partial x}$ in 3.26 is of first order in $\Delta x$. This means that the truncation error $O(\Delta x)$ goes to zero like the first power in $\Delta x$. This is the starter point to construct finite difference schemes. The main examples are, respectively, the forward difference scheme 3.27, the backward difference scheme 3.28, and the central difference scheme 3.29.

$$\left(\frac{\partial u}{\partial x}\right)_i = \frac{u_{i+1} - u_i}{\Delta x} + O(\Delta x) \tag{3.27}$$

$$\left(\frac{\partial u}{\partial x}\right)_i = \frac{u_i + -u_{i-1}}{\Delta x} + O(\Delta x) \tag{3.28}$$

$$\left(\frac{\partial u}{\partial x}\right)_i = \frac{u_{i+1} - u_{i-1}}{2\Delta x} + O(\Delta x^2) \tag{3.29}$$

It can be noticed that the truncation errors for the forward and backward differences are of first order, while the central difference yields a second order truncation error. Finally, we can derive the finite difference formula for the second derivative with second order accuracy,

$$\left(\frac{\partial^2 u}{\partial x^2}\right)_i = \frac{u_{i+1} - 2u_i + ui - 1}{\Delta x^2} + O(\Delta x^2) \tag{3.30}$$

In general, finite difference equations may be generated for any order derivative with any number of points involved if the solution is enough regular.

There are FDM schemes for typical elliptic, parabolic, and hyperbolic partial differential equations. Several physical conditions, for example viscosity, incompressibility and compressibility of the flow, affect the computational schemes. For incompressible flows the pressure-based formulation is provided, in order to keep from instability the pressure

field. This instability is due to the difficulties in preserving the balance equation when the sound speed becomes much higher than convection velocity components.

Furthermore, the incompressible flows, due to the difficulty to compute correct solution for pressure, are treated by two approaches: the primitive variable methods including, for example, the Semi-Implicit Method for Pressure Linked Equations (SIMPLE) and the Pressure Implicit with Splitting of Operators (PISO). The other approach is the vortex methods. It consists to eliminate from the momentum equations the pressure terms, which are computed by the vorticity transport equations.

### 3.2.2 Finite Volume Method

The finite volume method directly uses the conservation laws. Firstly, the space is divided into a number of control volumes.

$$\frac{\partial}{\partial t}\int_{V_i}\rho\phi dV + \int_{S_i} f^c \cdot n dS = \int_{S_i} f^d \cdot n dS + \int_{V_i} q_e dV \tag{3.31}$$

Then, the surface integrals of equation 3.31 are approximated by the sum of the fluxes crossing the face of the control volume. However, they are impossible to compute exactly. So, two approximation levels are provided: quadrature rules and interplotion. The scheme with which the flux is computed affects the accuracy of the spatial discretization.

Furthermore, there are two approaches in the definition of the shape and position of the control volume. As it is shown in Fig.3.4, in the *cell-centred scheme* the flow quantities are stored at the centroids of the grid cells, while in *cell-vertex scheme* at the grid points. For the first case the control volume is exactly equal to the grid cell. On the other hand, the union of cells sharing the grid point or some volume centred around the grid point determine the control volume in the cell-vertex scheme.

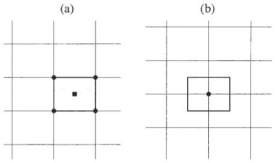


Figure 3.4: Control volume of cell-centred (a) and cell-vertex (b) scheme

There are several types of interpolation schemes, introduced in this Thesis in 1D:

- Upwind Difference Scheme (UDS)

  Upwind is a scheme that is more compatible with the advection process, i.e. dependent on the flow direction schematically displayed in Fig.3.5. The cell face values for the configuration are given by

$$\phi_e = \begin{cases} \phi_P & \text{if } \mathbf{v}\cdot\mathbf{n}_e > 0 \\ \phi_E & \text{if } \mathbf{v}\cdot\mathbf{n}_e < 0 \end{cases} \tag{3.32}$$

  This is equivalent to using a backward or forward difference for the first derivative. Because of its numerical diffusivity, this method never yield oscillatory solutions.

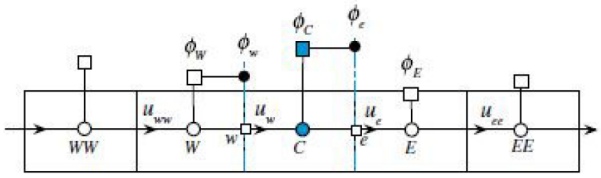


Figure 3.5: The upwind scheme profile

- Linear Interpolation (CDS)

  The value of $\phi$ at a face center is obtained performing a linear interpolation between the two nearest nodes.

$$\phi_e = \phi_E \lambda_e + \phi_P (1 - \lambda_e) \tag{3.33}$$

  where

$$\lambda_e = \frac{x_e - x_P}{x_E - x_P} \tag{3.34}$$

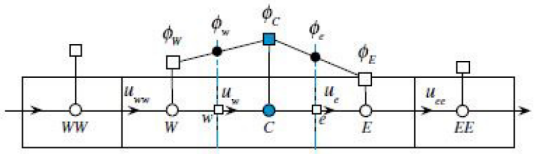


Figure 3.6: The CDS scheme profile

This scheme, displayed in Fig.3.6), is useful for non-directional problems, because it gives equal weights to the two nodes sharing the face.

- Quadratic Upwind Interpolation (QUICK)

  The Quadratic Upstream Interpolation for Convective Kinematics scheme, is based on interpolating the value of the dependent variable at each face of the element by using a quadratic polynomial biased toward the upstream direction, as shown in Fig.3.7. The interpolated value is used to calculate the convective term in the governing equations for the dependent variable.

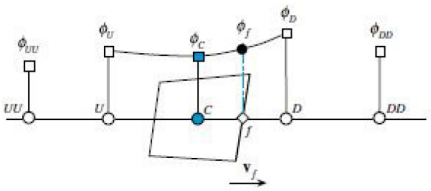


Figure 3.7: The QUICK scheme profile

Differently from the other cases, the variable $\phi$ is approximated by a parabola and one more point is needed to interpolate. This point depends on the upstream

direction. In fact, we will take W if the flow is from P to E ($u_x > 0$), EE if $u_x < 0$. The formula is

$$\phi_e = \phi_U + f_1(\phi_D - \phi_U) + f_2(\phi_U - \phi_{UU}) \tag{3.35}$$

where D,U and UU are the downstream, the first upstream and the second upstream node, respectively. The coefficients $f_1$ and $f_2$ are defined as

$$f_1 = \frac{(x_e - x_U)(x_e - x_{UU})}{(x_D - x_U)(x_D - x_U U)} \tag{3.36}$$

$$f_2 = \frac{(x_e - x_U)(x_D - x_e)}{(x_U - x_{UU})(x_D - x_{UU})} \tag{3.37}$$

### 3.2.3 Finite Elements Method

In Finite Elements Method (FEM) the domain is discretized in "elements", that are of various shapes. This leads us to generate irregular grids useful for complex geometries. Each element is composed by the connection of a defined number of nodes, depending on the type of the element and interpolation function. The main characteristic of the method, based on the so called "Method of Weighted Residuals", is that a weight function is used in the equations before being integrated over the whole domain. In general, the functions used to approximate the solution within each element are polynomial, because of their facility in integrations and derivatives. For example, a FEM solution can be approximated by a linear function, so that the continuity is guaranteed in each element. There are many possibilities for the approximated function and the weighted function. For example, in the Galerkin Method, the weight functions has the same form of the approximated function.

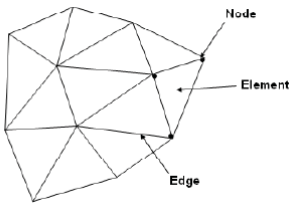


Figure 3.8: Typical two-dimensional Finite Element grid

### 3.2.4 Temporal discretization

For transient simulations, the governing equations are discretized even in time. In the temporal discretization we set up a time coordinate along which the derivative (for the finite difference method) or the integral (for the finite volume method) of the transient term is evaluated.

In general, a variable $\phi$ is expressed by an equation of the form

$$\frac{\partial(\rho\phi)}{\partial t} + \mathcal{L}(\phi) = 0 \tag{3.38}$$

where the function $\mathcal{L}(\phi)$ is a function that includes all non-stationary terms.

There are two basical methods to discretize the derivatives in time.

1. Explicit Method

   The transient first order explicit Euler scheme (Eq.3.39) is obtained by using a first-order "downwind" interpolation profile, where the new time is $t + \Delta t$ and that the functions of Eq.3.39 is computed at time $t$. Then, without solving linear systems, it is possible to evaluate the right hand side completely.

$$\frac{(\rho_C \phi_C)^{t+\Delta t} - (\rho_C \phi_C)^t}{\Delta t} V_C + L(\phi_C^t) = 0 \tag{3.39}$$

2. Implicit Method

   Even the implicit Euler scheme is obtained by using a first-order "upwind" interpolation,.

$$\frac{(\rho_C \phi_C)^t - (\rho_C \phi_C)^{t-\Delta t}}{\Delta t} V_C + L(\phi_C^t) = 0 \tag{3.40}$$

   So, it seems that this method is not efficient as the Explicit method beacuse a linear system for each time step is needed to solved. However, in opposite with the explicit method, the Implicit one is the unconditional stability of the temporal scheme. On the other hand, the explicit method is *unconditionally unstable*. This leads to impose restrictions on the time step to guarantee the stability. This feature is well explained by the *Courant number*, a dimensionless parameter defined as the ratio between the time step, $\Delta t$, and the characteristic convection time, $u/\Delta x$. Then, in order to guarantee the stability, we can obtain the *Courant-Friedrichs-Lewy* condition (CFL),

$$\Delta t < \frac{\Delta x}{|u|} \tag{3.41}$$

   where $u$ is the flow speed, $\Delta t$ the time step and $\Delta x$ the spatial length

# Chapter 4

# Numerical methods in CWE: Computation grid generation

At this point, it is needed to define the geometry. Usin ANSYS Workbench it is possible to realize a simple geometry or to import this with a CAD program. In order to obtain correct results, it is important to generate correctly the calculation domain.

## 4.1 Mesh Types

One of the most important characteristics in CWE simulations is to generate the mesh. It means to discretize the spatial domain in small cells connected between them, so that we can compute the variables with numerical methods. A fine mesh can be related to the computational cost, the accuracy and convergence of the solution. Generally, there are three types of meshes (Fig.4.1):


Figure 4.1: Types of grids

- Structured mesh
  It is identified by regular connectivity between the elements and it is composed by elements like quadrilateral in 2D and hexahedra in 3D. A good characteristic is that space is divided with such efficiency. In fact each point can be defined by indexes

($i$,$k$,$k$) in the cartesian coordinate system, so that the neighborhood relationships are defined by storage arrangement. In addition, we can have an orthogonal or non-orthogonal mesh. A structural mesh will be non orthogonal if the lines do not intersect perpendicularly, in opposit with the orthogonal grid. However, a disadvantage is that in complex geometries it is difficult the implementation of this types of mesh.

- Unstructured mesh
  On the other hand, the characteristic of unstructured mesh the irregular connectivities between the elements. It is easy to generate from an algorithm of the program. Of consequence, the nodes are not ordered and we can not identify these by indexes. A mix of quadrilaterals and triangles elements are generally used in 2D simulations, while tetrahedra and hexahedrons in 3D problems. Then, the main advantage of unstructered grids is that the complex geometry can be easily discretized. However, we have to be careful to get a suitable mesh beacuse it is easy to generate a bad quality grid. In addition, a large amount of space can take up in the memory of the computer.

- Hybrid mesh
  As the name suggests, this type of mesh is a efficiently combination between structured and unstructured meshes. It is adapt in an irregular domain, so that the structured grids can be used regular region, while in complex areas it is convenient to use unstructured meshes.

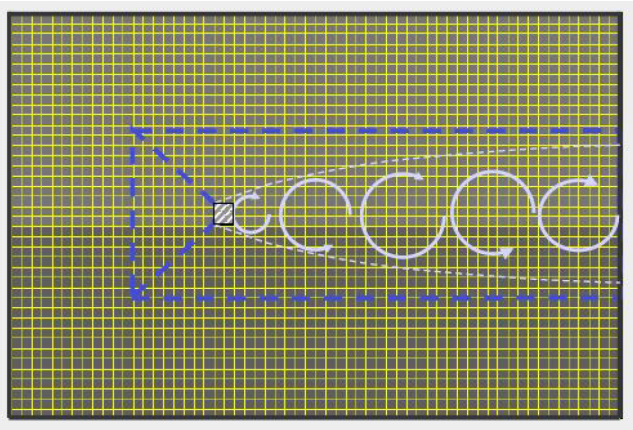

Figure 4.2: Structured, orthogonal and equi-spaced grid

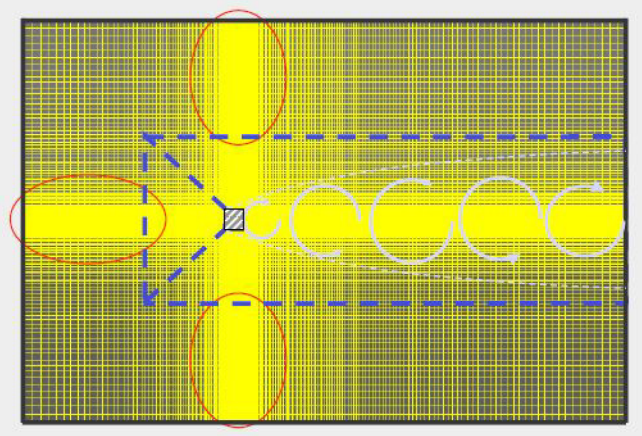

Figure 4.3: Structured, orthogonal and non equi-spaced grid

In application of a square cylinder domain, we can see examples of type grids explained above. In Fig.4.2 the grid is structured, orthogonal and equi-spaced. It conduce to poor accurate simulation in zones with high gradients, but computational cost are reduced (only 2396 CV). In opposite, in Fig.4.3, we have a structured, orthogonal, but non equi-spaced grid. In the wake and in wall zone the simulation is accurate. However, the discretization is exaggeratedly fitted in regions less important. Moreover, computational cost are very high. (28800 CV generated).

So, in order to provide a better simulation with computational cost contained, in Fig.4.4 we have a boundary-fitted, structured, non-orthogonal and non equi-spaced grid (only 3840 CV). It is used in aerodynamics on profiled body. However, this grid is poor precise in the wake, and quality grid is reduced, because of non-orthogonality, skewness and high factors of grid stretching. Then, a boundary-fitted, unstructured, non-orthogonal, and non equi-spaced grid shown in Fig.4.5 is the best grid with high resolution in regions with elevate gradients and coarse in less critical regions. It leads to limit the computational cost (20672 CV). Also, grid stretching is reduced. However, it is necessary to generate automatically the grid with robust algorithm, that have to pay attention to the quality grid.

In the next section, grid induced errors are introduced including non-orthogonal, skewness and grid stretching errors mentioned above.

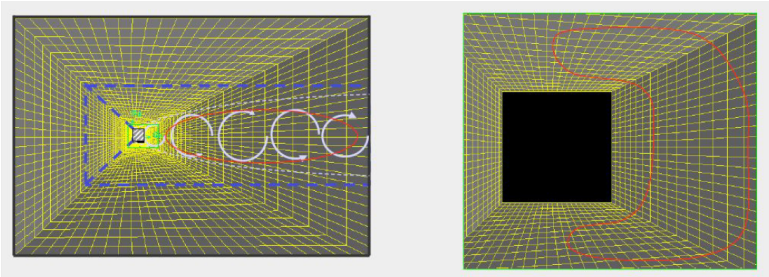

Figure 4.4: Boundary-fitted, structured, non-orthogonal and non equi-spaced grid

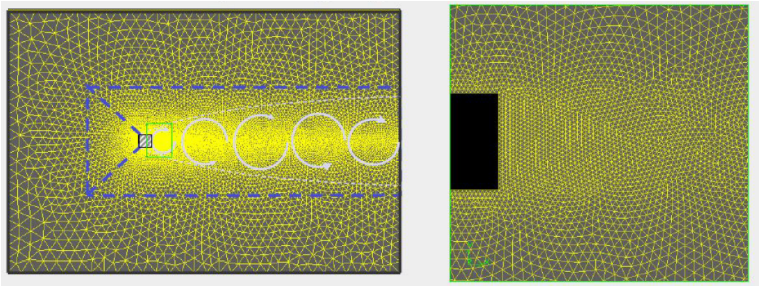

Figure 4.5: Boundary-fitted, unstructured, non-orthogonal and non equi-spaced grid

## 4.2 Grid induced errors

Grid induced errors are dependent on two main factors: mesh resolution and grid quality.

Insufficient mesh resolution can lead to lose effectively the shape of the solution, in particularly if the solution changes rapidly in some regions of the domain and the local number of computational points is not sufficient to describe that change. Moreover, it should be note that must exist a balance between the size of the cells and the computational cost of the simulation.

Discretization of complex geometries can lead to let down the grid quality. Mesh quality is a property of the mesh, independent from the particular problem to solve. Grid quality errors can be higher than errors derived from the model and interpolation. On the other hand, a better quality mesh can reduce discretization error of the same order, or greater, than a refinement grid. So, the improvement of a mesh grow drastically computational efficiency in rapport to accuracy and cost. Finally, the quality of the mesh is judged by the level of grid induced errors caused by the aspect ratio, non-orthogonality and mesh skewness.

- Aspect Ratio

  The aspect ratio is known as a measure of the stretching because it is defined as the ratio of the maximum distance between the cell and face centroids to the minimum distance between the nodes of the cell. Ideally, it should be equal to 1 to ensure the best results. Moreover, the local variation in cell size should be minimal, it means the adjacent cell should not have an increase of aspect ratio higher than 20%.

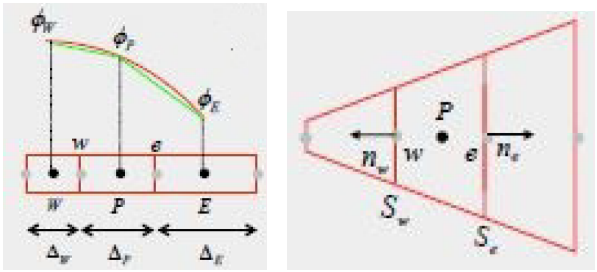


(a) (b)

Figure 4.6: Gradient grid on x (a) and y (b) direction

- Orthogonality

  It is referred to the angle, $\theta$, between the line which connects the nodes of adjacent cells and the normal vector of the face dividing these relative cells. In 1D, the orthogonality of the grid is always verified but in 2D, it could not be. To obtain good results, this angle $\theta$ should approach to zero.

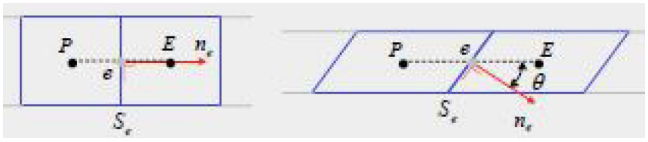


Figure 4.7: Orthogonality (on the left) and Non-orthogonality (on the right) on the face.

- Skewness

  The distance $m$, Fig. 4.8, between the middle point of the face and the line which joins the nods of the two adjacent cells is defined as skewness.

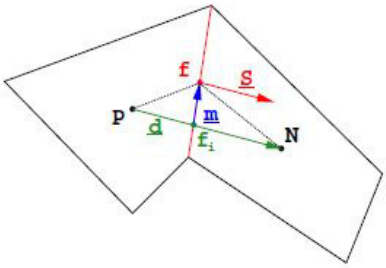


Figure 4.8: Skewness error on the face.

### 4.2.1 Grid stretching error

Grid stretching error is strongly correlated with grid gradients. In the evaluation of the diffusion term with CDS, we have grid gradient along x, where the approximation of first order of the derivative along $x$ on quadrature point is

$$\left(\frac{\partial\phi}{\partial x}\right)_e = \frac{\phi_E - \phi_P}{x_E - x_P} + \frac{(x_e - x_p)^2 - (x_E - x_e)^2}{2(x_E - x_p)}\left(\frac{\partial^2\phi}{\partial x^2}\right)_e + H \tag{4.1}$$

while grid gradient along $y$ leads to an approximation of second order. In addition we have errors on flux at the $w$ and $e$ faces ($S_w < S_e$) that are not compensated.

$$F_{d,x} = \int_{S_w} \Gamma\left(\frac{\partial\phi}{\partial x}\right)_w n_w dS_w + \int_{S_e} \Gamma\left(\frac{\partial\phi}{\partial x}\right)_e n_e dS_e \tag{4.2}$$

### 4.2.2 Non-orthogonal error

The diffusion term is strictly affected by grid induced errors. Discretizing the diffusion term, it follows:

$$F^d_{CV} = \sum_{f=1}^{n} \Gamma S(\nabla\phi)_f \tag{4.3}$$

where

$$S(\nabla\phi) \approx |S|\frac{\phi_N - \phi_P}{|d|} \tag{4.4}$$

in the case of orthogonal grid.

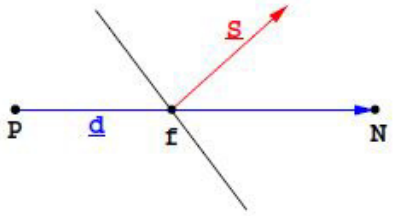


Figure 4.9: Vectors $d$ and $S$ on a non-orthogonal mesh

If the grid is not orthogonal, $S$ can be written as

$$S(\nabla\phi) = \Delta(\nabla\phi)_f + k(\nabla\phi)_f \tag{4.5}$$

where

$$\Delta(\nabla\phi)_f = |\Delta|\frac{\phi_N - \phi_P}{|d|} \tag{4.6}$$

is the orthogonal term, and

$$k(\nabla\phi)_f = k(\lambda(\nabla\phi)_P + (1-\lambda)(\nabla\phi)_N) \tag{4.7}$$

is the non-orthogonal correction. From the several possibile decomposition, the minimum correction approach keep the non-orthogonal correction as small as possible. So, $\Delta$ and $k$ are orthogonal:

$$\Delta = \frac{dS}{dd}d \tag{4.8}$$

. Then, greater is the non orthogonality, lower is the orthogonal term.

### 4.2.3 Skewness error

*Skewness error* is a numerical diffusion-type error. In Fig. 4.8 it is shown a general situation causing the skewness error. However, skewness grid is not necessarily related to the non-orthogonality. The computations of face integrals requires the value of the variable in the middle of the face (point $f$ in Fig. 4.8):

$$\int_f dS\phi = S\phi_f \tag{4.9}$$

The linear interpolation of the value from the point $P$ and $N$ around the face gives $\phi_f$. However, the value of $\phi$ refers to the point of $f_1$, which is not necessarily in the middle of the face. So, the face integral, from the second order, reduces to first order accuracy. For the convection term, for a generic CV we have

$$F_{CV}^{c} = \nabla(\rho U \rho) = \sum_{f=1}^{n} S(\rho U \rho)_f \tag{4.10}$$

in no skewness case,

$$F_{CV}^{c} = \nabla(\rho U \rho) = \sum_{f=1}^{n} S(\rho U \rho)_{f_{sk}} \tag{4.11}$$

in skewness case. These leads to the error term

$$E_{V}^{c} = \sum_{f=1}^{n} S(\rho U \delta\rho)_f \tag{4.12}$$

with $\delta\phi_f = \delta_f - \delta_{f_{sk}} = m(\nabla\phi)_f$. It can be written

$$E_{V}^{c} = \nabla(\Gamma_{sk} \nabla\phi) \tag{4.13}$$

where $\Gamma = (\rho U)_f m$ is skewness diffusive coefficient. This coefficient is proportional to the $m$ value. It means that if $m$ is greater, even $\Gamma_{sk}$ is bigger. So, the skewness error have diffusive type. In this Thesis, this error will be deeply study to prove a relation to the inaccurate solutions.

### 4.2.4 Quality index

Quality grid error is reducible by refinement. As shown in Fig. 4.10(a), we can see how the skewness error is dropped.

Another method to reduce quality grid error is to grow quality mesh (CV type, geometric characteristic) as shown in Fig. 4.10(b)-(c). So, it is useful to define a metric in order to evaluate a grid.

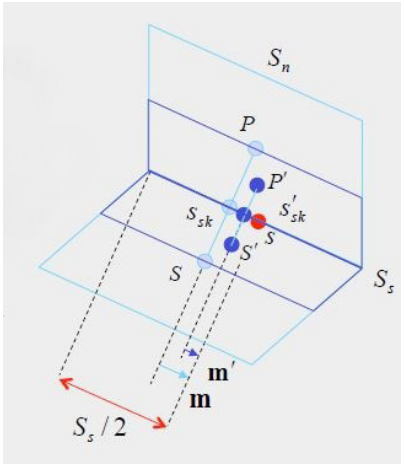


(a) Reduction of skewness error by refinement

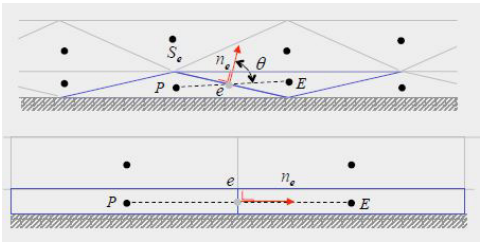


(b) Example of a better grid quality

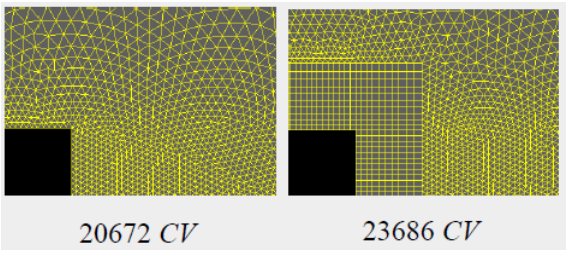


(c) Reduction of non-orthogonality error with hybrid grid (quad and tri)

Figure 4.10: Example of reduction of grid quality error

Generally, for all elements and for all geometric characteristic, there are no significant quality indicators. However, we can define some metric. For example, as shown in Fig. 4.11(a), a good measure for orthogonality is

$$Q_{AR} = \frac{1}{2}\frac{R}{r} \geq 1 \tag{4.14}$$

where if $Q_{AR} = 1$ we have an equilateral triangle. But it is useful only for triangle grids. So, an alternative would be

$$Q_{ER} = \frac{\max(s_1, s_2, ..., s_n)}{\min(s_1, s_2, ..., s_n)} \geq 1 \tag{4.15}$$

where $s_i$ is shown in Fig. 4.11(b). As in $Q_{AR}$, if $Q_{ER} = 1$ the cell is equilateral.

A metric that can be associated with the skewness, even it is not rigorous, is the *equi*

*angle skewness*, Fig. 4.11(c) defined as:

$$Q_{EAS} = \max\Big(\frac{\theta_{\max} - \theta_{eq}}{180 - \theta_{eq}}, \frac{\theta_{eq} - \theta_{\min}}{\theta_{eq}}\Big) \tag{4.16}$$

where

$$0 \leq Q_{EAS} \leq 1 \tag{4.17}$$

and $\theta = 60°$ for triangles and $\theta_{eq} = 90°$ for quadrilateral grids. However, if $Q_{EAS}$=0 we have an equi-angle triangle.

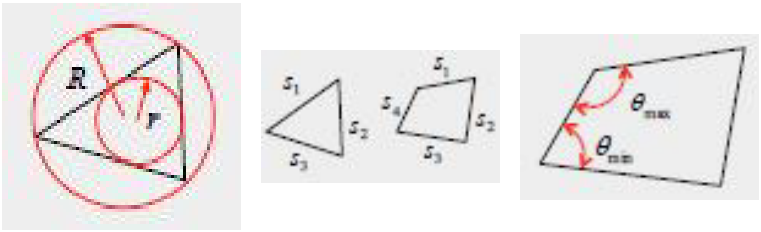


(a) (b) (c)

Figure 4.11: Aspect ratio (a), edge ratio (b) and cell equiangle skewness (c)

This measure is provided by commercial software as Fluent, so that we can easily compute this index for each different mesh. On the other hand, we have to keep in mind that this measure is not totally reliable. It doesn't capture as well the skewness. For example, we can see in Fig. 4.10(b) a non-orthogonal grid with no skewness. Nevertheless, *cell equiangle skewness* is not 1 as it should be an ideal metric. So, cell equiangle skewness involves even cells with no skewness error. This is important because we will use this measure in order to find a correlation between this metric and gradients velocity. The results could not be efficient as we except.

# Chapter 5

# Building the model

In this chapter, we will explain the necessary steps to define and solve computationally the problem investigated in this Thesis.

## 5.1 Physical and computational description

As we have already mentioned, the flow past a square cylinder has been chosen beacuse of its importance in some fields. In fact, there are many literato so that we can compare the results. Finally, its computational set-up is not too difficult. In this section, we show the main parameters defined and, in the next one, we will be focused only in the central part of this Thesis, the mesh.

### 5.1.1 Geometry

*DesignModeler* tool, included in ANSYS leads us to define the geometry shown in the Fig. 5.1, where the dimensions of the different domains are included. Moreover, it is symmetric respect to x-axis.

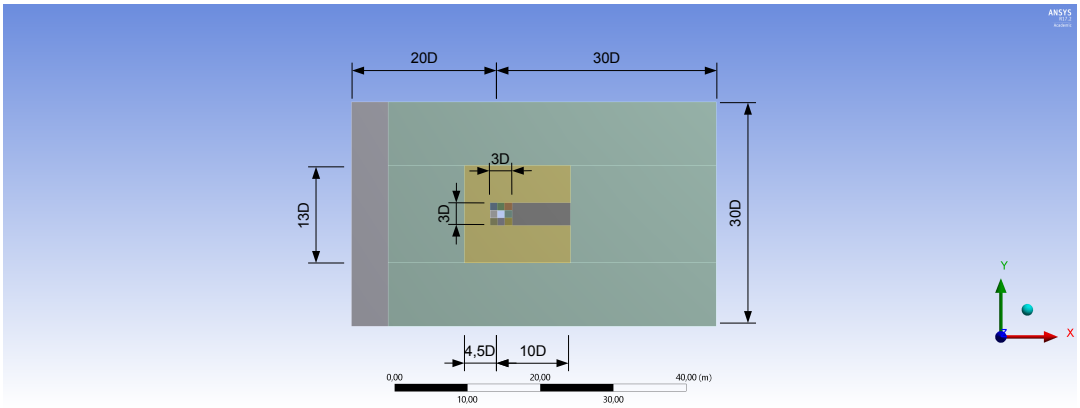


Figure 5.1: Geometry model

Furthermore, in the Fig. 5.2 the domains are defined from out to inside as *outer ring*, *middle C*, *wake* and *inner ring*. In this last region, we will analyze the flow simulation.

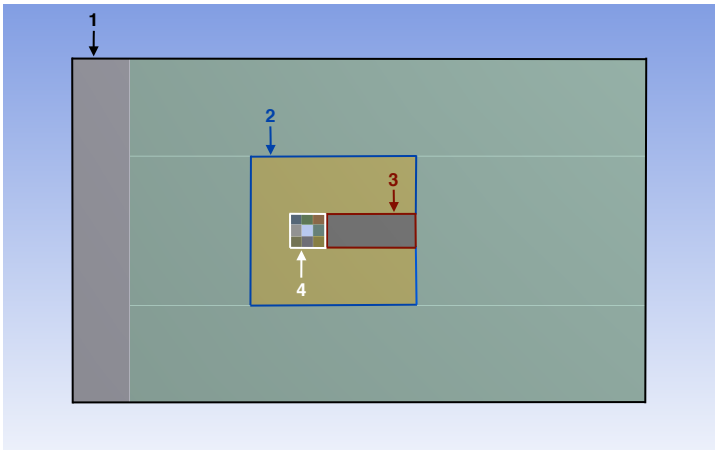


Figure 5.2: Domains

At this point, it should be built the mesh, that in the next section will be discussed.

### 5.1.2 Model and boundary conditions

In order to solve the problem, the RANS $k-\epsilon$ model, described in the Chapter 3, is used in this Thesis, where $k$ is the kinetic energy and $\epsilon$ the dissipation, both parameters of the turbulence.

In addition, we will work with a transient air flow, which is transfered with a high Reynolds number ($Re = 2.2 \cdot 10^4$). This flow moves in a 2D space and its dimensionless properties are defined as:

$$\rho = 1$$

$$\nu = \frac{1}{Re} \approx 4.54 \cdot 10^{-5}$$

Furthermore, the boundary conditions are so defined in Fluent:

| Boundary condition | Type | Characteristics |
|---|---|---|
| Cylinder | Wall | Non-slip condition. |
| Inlet | Velocity inlet | It is defined only the x-component of velocity at the inlet. Turbulent intensity and length scale are, respectively, set to 2% and 0.5 |
| Lateral | Symmetry and Periodic | Within periodic type, we impose a traslational motion. |
| Outlet | Pressure outlet | Dirichlet condition: $p_{rel} = 0$ and the direction of the flow normal to the boundary. This boundary condition should be imposed far enough from the cylinder so that the flow solution across the cylinder is not affected by the outlet condition. In addition, turbulence intensity and length scale has equal to those defined in the *inlet boundary condition*. |

Table 5.1: Boundary conditions

### 5.1.3 Solution Methods

In order to discretize and resolve this problem, in the following we have imposed these numerical methods and solver:

- **Solver:** Pressure-Based.
- **Pressure-Velocity coupling:** PISO with *Skewness Correction* and *Neighbor Correction* both equal to 2 only in the non-orthogonal grids, while set to 1 in the others.
- **Spatial discretization**
  - **Gradient:** Least Squares Cell Based.
  - **Pressure:** Second Order.
  - **Momentum:** QUICK.
  - **Turbulent Kinetic Energy:** QUICK.
  - **Turbulent Dissipation Rate:** QUICK.
- **Transient Formulation:** Second Order Implicit (Euler method).

Finally, the *Residuals* define the convergence ratio. Normally, to avoid errors induced by the solver, this value is small enough, 0.001.

Moreover, aerodynamics coefficients, i.e. *lift* and *drag*, are stored in different files for each grid type. So, it is useful to save correctly the results of the simulations defining the number of time steps.

## 5.2 Mesh description

In this section, there are described the steps to build the mesh necessarly to solve our simulation. In particular, the *Inner ring-grid* will be deeply analyzed.

After the creation of the geometry, the mesh can be generated. Next, we can define the turbulence model. We use the tool *Meshing* included in ANSYS. Four regions divide the simulation domain (Fig. 5.2). Then, for each part, a distinct type of mesh has been defined: firstly, the *Outer ring-grid* is generally structured but unstructured in the rear part, across the wake. Secondly, a triangular unstructured mesh define the *Middle C-grid*. Thirdly, the *Wake grid* is totally structured orthognal. Last, but not least, *Inner ring-grid* is the most important zone in this study. We have generated seven typres of grids for this region (Fig. 5.5) in order to analyze deeply the inaccurate solution affected by a low quality mesh.

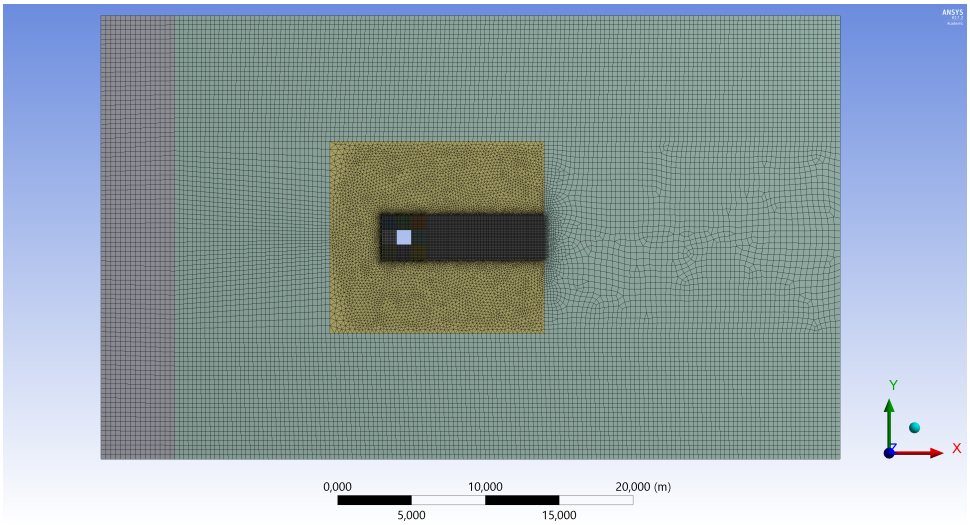


Figure 5.3: Mesh

In order to generate these seven grids, we have to define several conditions that are stored in the table 5.2. As it is shown in the Fig. 5.4, each line of the domain is referred by a letter. Next, we divide the edge defining the number of divisions and the bias type. This last option, if it is active, means that we should impose a bias factor that is defined as the total expansion ratio of the cells in this side. On the other hand, a hard behavior option leads to fixed the size or number of divisions. This is imposed in all the cases.

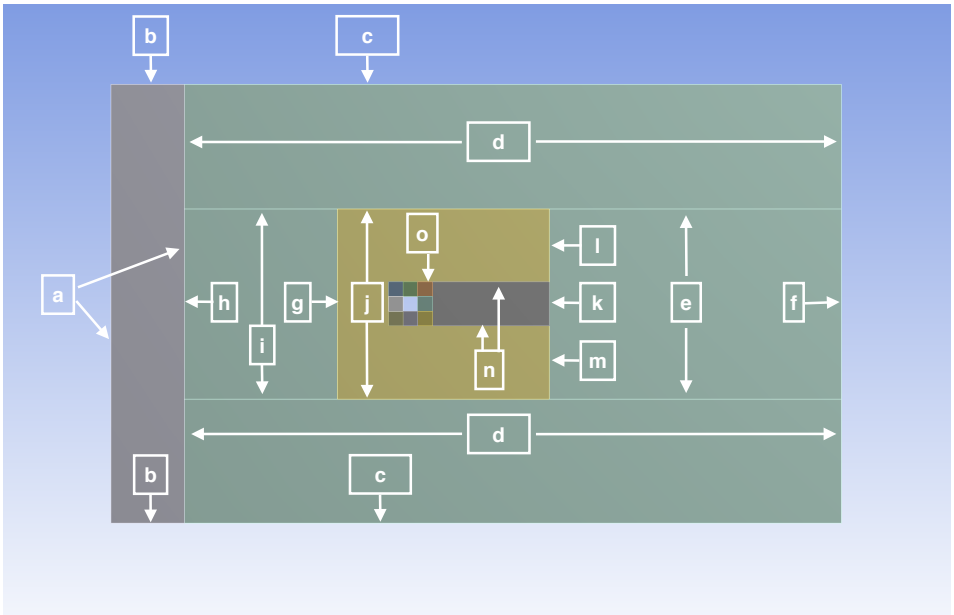


Figure 5.4: References to create the meshes

| Label | Bias type | Number of elements |
|---|---|---|
| a | no | 94 |
| b | no | 15 |
| c | no | 150 |
| d | no | 27 |
| e | no | 66 |
| f | no | 30 |
| g | ... .. . .. ... $fct = 3$ | 40 |
| h | no | 40 |
| i | no | 36 |
| j | no | 48 |
| k | no | 72 |
| l | . .. ... $fct = 3.5$ | 30 |
| m | ... .. . $fct = 3.5$ | 30 |
| n | no | 160 |
| o | no | 24 |

Table 5.2: Characteristics of each edge

The different types of mesh generated in the *Inner ring* is shown in the Fig. 5.5. We have the *structured orthogonal*, *structured non orthogonal*, *structured/unstructured*, *unstructured*, *structured downwind non orthogonal*, *structured upwind non orthogonal* and *structured top non orthogonal* mesh. The grids of the others sections are equal. So, the results for the different cases can be compared only in the inner ring.

Firstly, in the *structured orthogonal* mesh, eight surfaces divide the *Inner ring*. The number of divisions imposed to each edge of these surfaces are 24.

Secondly, in the *structured non orthogonal*, the *Inner ring* is always divided into eight surfaces, but the features are different. In order to keep a structured mesh in the *wake*, we have to define the number of elements on the left and right sides are equal to 72. Furthermore, on the diagonal edges, we impose a number of divisions equal to 24.

Thirdly, the *structured/unstructured* mesh has the same procedure as in the *structured* mesh, but and four zones are *unstructured*. To generate these regions, 24 elements divide each edge, but no mapped face are imposed.

Next, the *unstructured* mesh is built. In this case, the external edges of the *Inner ring* are divided into 72 elements and, in the cylinder sides, we impose a number of elements equal to 24. In order to keep the mesh symmetric respect to x-axis, we have imposed this number of divisions even in the diagonal edges. As in the unstructured zones of the *structured/unstructured* mesh, no mapped face are set up.

Finally, the last three grids are combination of the first two ones. However, the *Inner ring* is divided into nine surfaces in order to keep the non-orthogonal zone in one half part of the inner grid. *Structured upwind non orthogonal* mesh has non-orthogonal region in the upwind zone, while *structured downwind non orthogonal* mesh in the downwind zone. On the top of the inner grid, *structured top non orthogonal* has the non-orthogonal region there. These localization of the non-orthogonal region could be suggest us which zone has a critical impact on the solution.

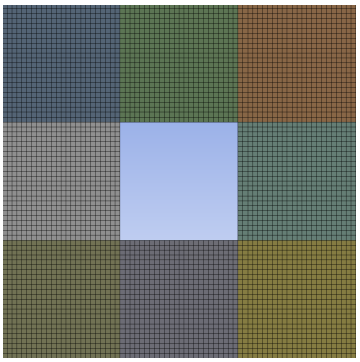

(a) Structured orthogonal

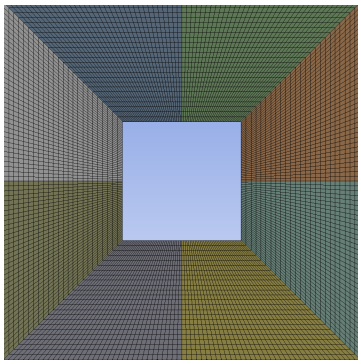

(b) Structured non orthogonal

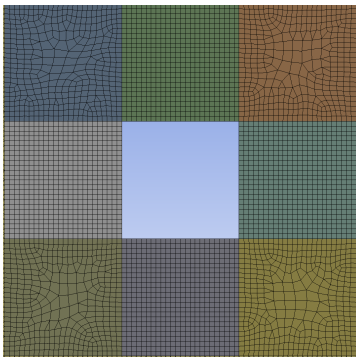

(c) Structured/Unstructured

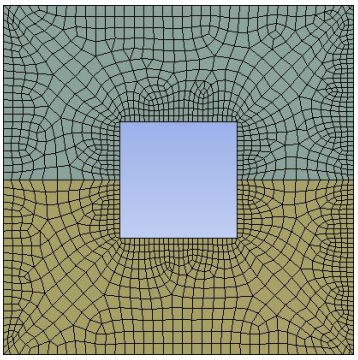

(d) Unstructured

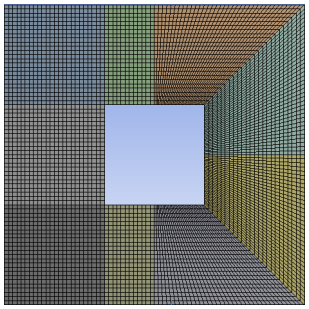

(e) Structured downwind non orthogonal

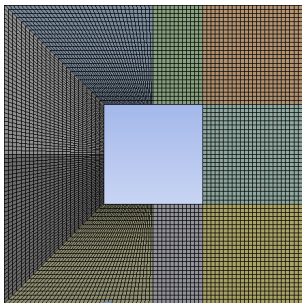

(f) Structured upwind non orthogonal

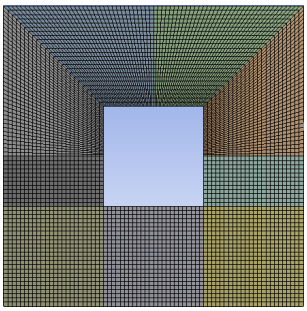

(g) Structured top non orthogonal

Figure 5.5: Inner ring grids

## 5.3 Mesh quality

In this section we are going to show the quality parameters, explained in Chapter 4, of the seven types of grids defined before: Aspect Ratio, Non-orthogonality and Cell Equiangle Skewness.

| Mesh | Max. Aspect Ratio | Min. Orthogonality | Max. Skewness |
|---|---|---|---|
| Structured Orthogonal | 4.85855 | 4.81664e-01 | 3.23771e-01 |
| Structured Non Orthogonal | 6.81491 | 4.81664e-01 | 4.04156e-01 |
| Structured/Unstructured | 5.19822 | 4.81664e-01 | 3.50503e-01 |
| Unstructured | 9.66749 | 2.87338e-01 | 8.082429e-01 |
| Structured Downwind Non Orthogonal | 7.21231 | 4.02806e-01 | 8.082429e-01 |
| Structured Upwind Non Orthogonal | 7.79483 | 2.59453e-01 | 7.235305e-01 |
| Structured Top Non Orthogonal | 1.13426e+01 | 3.36381e-01 | 7.584536e-01 |

Table 5.3: Mesh quality

The table 5.3 collects the *aspect ratio*, the minimum *orthogonality* and maximum *skewness* values of the parameters related to *mesh quality*. Both *orthogonality* and *skewness* values goes from 0 to 1. On the one hand, if the value is near to zero, it means that the mesh has a low quality. On the other hand, the values near to 0 correspond to a high quality in the *skewness* case. In general, for the *aspect ratio*, where the flow field exhibit strong gradients, it is better to avoid sudden changes. We can see in table 5.3 high maximum value of *aspect ratio* in all the meshes. This is probably due to the abrupt change of the cell size between the wake and the rear part of the outer ring. Furthermore, in order to not lose the main information, we have generated the wake domain sufficiently long. So, the effect of *aspect ratio* can be considered negligible in the solution. Finally, if we look into to the *orthogonality* values, we can see they are similar. This leads us to think that the *non-orthogonality* has an effect in the error of the solution, but it probably will be the same in all meshes and we can not consider it. The only parameter which is different for each grid is the *skewness*.

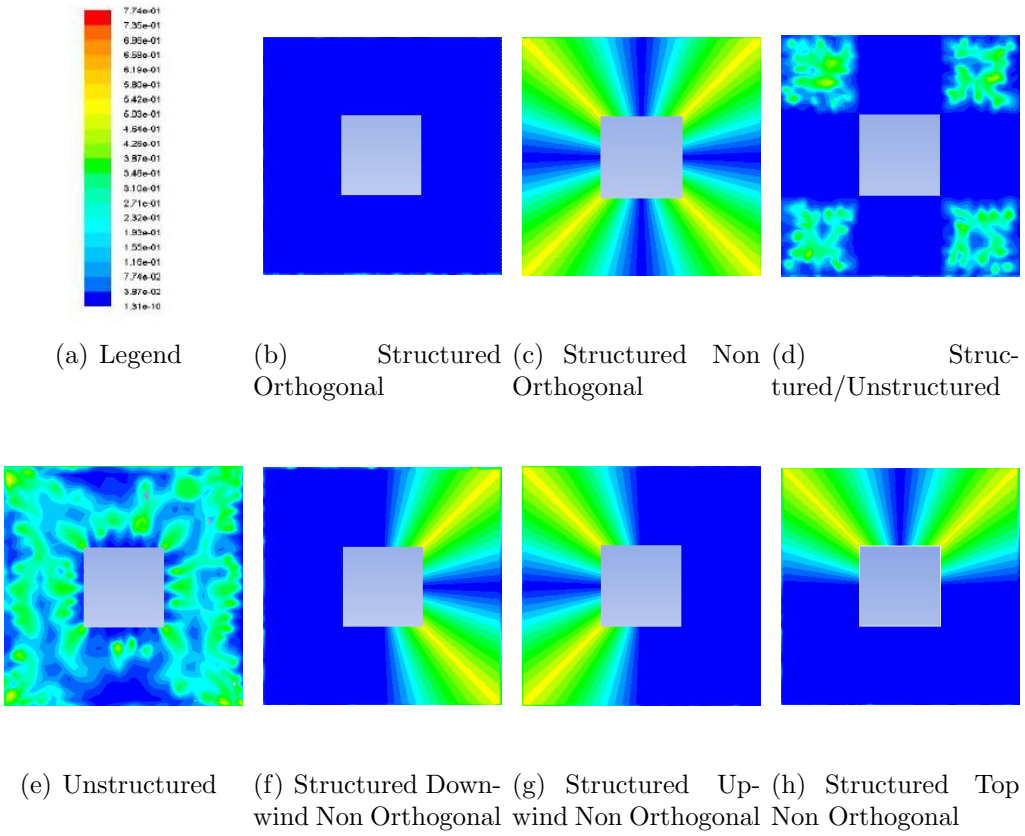

(a) Legend (b) Structured Orthogonal (c) Structured Non Orthogonal (d) Structured/Unstructured

(e) Unstructured (f) Structured Downwind Non Orthogonal (g) Structured Upwind Non Orthogonal (h) Structured Top Non Orthogonal

Figure 5.6: Skewness contours

In the Fig. 5.6, the various skewness contours have been shown, where we can see the scale of colors used with the corresponding values. Blue color is referred to low value of cell equiangle skewness, while red color to highest values. The structured meshes appear completely colored blue as we expect. In all the non-orthogonal mesh, we observe a variation of colors from navy blue to yellow. In particular yellow color are present on the diagonal where the distortion of non-orthogonal grids is much higher. Moreover, the *unstructured* mesh have almost all colors in a distributed way.

To define which mesh has a larger skewness factor, the percentage data have been collected for each part of the domain in all cases and they have been plotted in the following histograms.

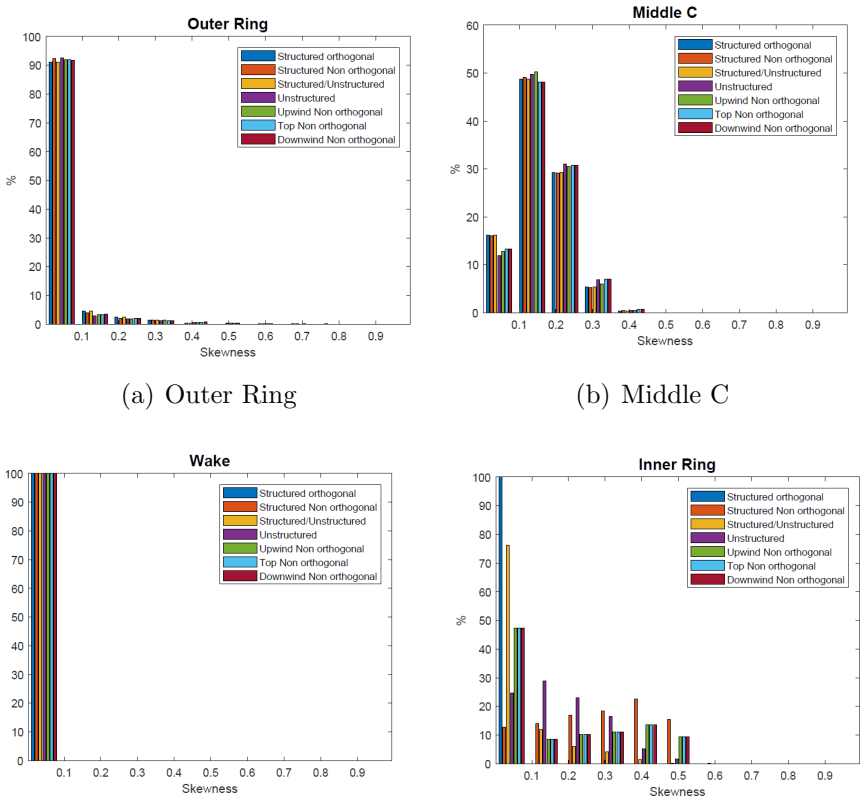


(a) Outer Ring

(b) Middle C

(c) Wake

(d) Inner Ring

Figure 5.7: Histograms

As we can see in the figures 5.7 (a), (b) and (c), generally, the skewness values concide approximately for the four cases, as we expected. Theoretically, the *outer ring*, *middle C* and *wake* grids should be the same for all cases. However, some variances can appear according to the direction in which FLUENT generates the mesh. Finally, the value of the skewness for the *structured orthogonal*, *structured non orthogonal*, *structured/unstructured* and *unstructured* mesh is different, as it is shown in the figure 5.6 (d). The worst results are obtained for the *structured non orthogonal* grid. It is because its higher values of skewness ($\sim 0.4$) are related to the largest percentage value of total elements ($\sim 20\%$). In the second place, the *unstructured* grid is located. The highest percentage of elements near to 20% has a skewness value of 0.1. In the case of the *structured/unstructured* mesh, most of the elements have a skewness value approximate to 0.05 because of the effect of the structured meshes. Last but not least, the *structured* mesh have all the elements with the minimum skewness.

# Chapter 6

# Postprocessing: Results Analysis

In this chapter, we will discuss all the results of interest that can be obtained in the *Postprocessing*. The main objective of this Thesis is to show that the quality grid can be affect the solution.

## 6.1 Aerodynamic Coefficients

The first quantities of interest are the *Aerodynamics Coefficients* as *Lift* and *Drag coefficients*. They can be expressed, respectively, as

$$C_L = \frac{L}{\frac{1}{2}\rho V^2 D} \tag{6.1}$$

$$C_D = \frac{D}{\frac{1}{2}\rho V^2 D} \tag{6.2}$$

where $D$ is the reference length of the square cylinder.

In Fluent, these coefficients can be easily calculated. After we have defined the same time step in all grids, $\Delta t = 0.02$, and a number of iterations equal to 12000 so that we make sure to have in all cases a steady flow, we can plot each *aerodynamic coefficient* for all the seven mesh and compare them.

First of all, the mesh that gives the most accurate solutions according with the literature is the *structured orthogonal* mesh with a $CL$ value near to 1.5 So, it can be considered as a reference for the other grids that we analyze. For a better visualization we have chosen to show the results dividing in two groups. In the first group, as we can see in the Fig. 6.1 and 6.3, there are the reference grid (*structured orthogonal*), *structured non orthogonal*, *structured/unstructured* and *unstructured* meshes. In the other group, as shown in Fig. 6.2 and 6.4 the reference grid too, *structured downwind non orthogonal*, *structured upwind non orthogonl* and *structured top non orthogonal* meshes. Even in the next figures we will use this visualization.

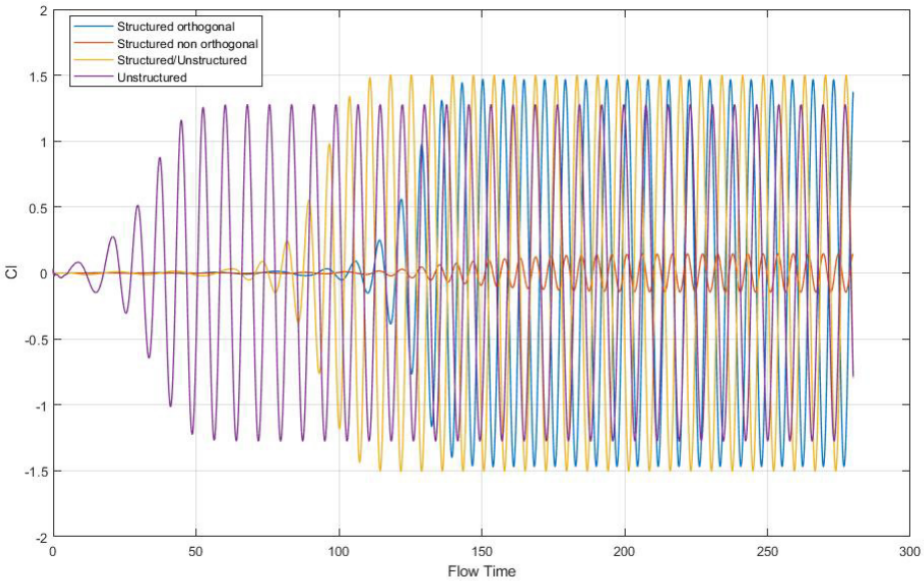


Figure 6.1: Lift coefficient for structured orthogonal, structured non orthogonal, structured/unstructured and unstructured

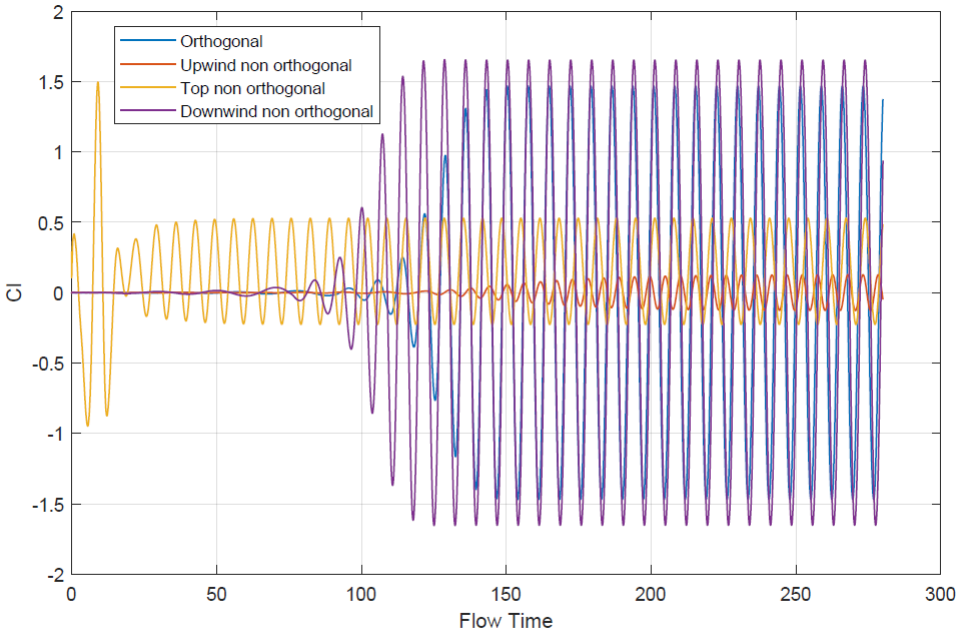


Figure 6.2: Lift coefficient for structured orthogonal, downwind, upwind and top non orthogonal

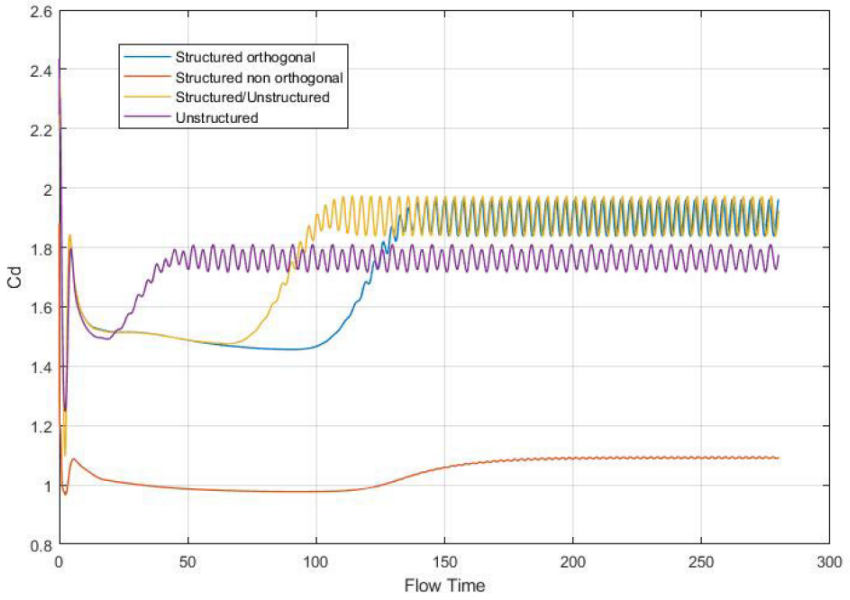


Figure 6.3: Drag coefficient for structured orthogonal, structured non orthogonal, structured/unstructured and unstructured

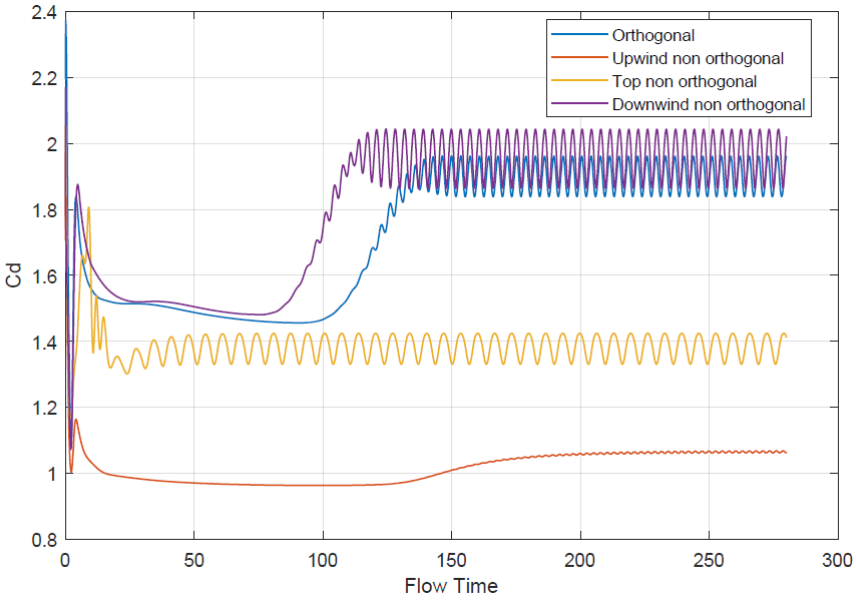


Figure 6.4: Drag coefficient for structured orthogonal, downwind, upwind and top non orthogonal

As we can see in the previous figures, the meshes that have results nearer to the reference grid are the *structured/unstructered*, *unstructured* and *structured downwind non orthogonal*. While the unstructured mesh underestimate the results of $CL$ and $CD$, the

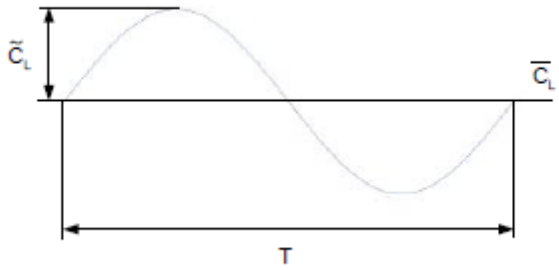


Figure 6.5: Representation of a period, average and maximum lift

| Mesh | $\overline{C}_L$ | $\tilde{C}_L$ | $\overline{C}_D$ | $\tilde{C}_D$ | $T$ | $St$ |
|---|---|---|---|---|---|---|
| Structured Orthogonal | 0 | 1.4664 | 1.900 | 1.9616 | 7.22 | 0.139 |
| Structured Non Orthogonal | 0 | 0.1455 | 1.0916 | 1.0945 | 5.28 | 0.189 |
| Structured/Unstructured | -0.002 | 1.4989 | 1.9035 | 1.9709 | 7.26 | 0.138 |
| Unstructured | -0.003 | 1.2762 | 1.7631 | 1.8090 | 7.74 | 0.130 |
| Structured Downwind Non Orthogonal | 0 | 1.6519 | 1.9612 | 2.0426 | 7.26 | 0.138 |
| Structured Upwind Non Orthogonal | 0 | 0.1267 | 1.0656 | 1.0688 | 5.24 | 0.191 |
| Structured Top Non Orthogonal | 0.15 | 0.5286 | 1.3849 | 1.4244 | 6.62 | 0.151 |

Table 6.1: Maximum and averaged coefficients

downwind non orthogonal mesh overestimate these quantities. Moreover, in these meshes the flow becomes faster steady rather than the reference grid. On the other hand, *structured non orthogonal* and *upwind non orthogonal* grids have a stationary flow very later rather than the other meshes. Furthermore, the last two grids provide a completely wrong result with a $CL$ value near to 0.15, an order of magnitude under the correct value. Even the *top non orthogonal* grid has a lower value of both aerodynamic coefficients. However, the mean $CL$ is not 0 as the other grids, beacuse the mesh is not symmetric. For drag coefficient, we can see in *unstructured* case a non-periodic feature.

In addition, in the following table (6.1) there are collected the maximum ($\tilde{C}_L$) and average ($\bar{C}_L$) aerodynamic coefficients. There are also in the table the period $T$, represented in Fig. 6.5 and the Strouhal number $St$. In a dimensionless model $St = 1/T$. As it was observed before, the average value of the lift coefficient is different from zero when the mesh is *top non orthogonal*. The average drag coefficient is not zero in all cases. The reference grid have mean drag coefficient equal to 1.9, and this is near to the experimental data.

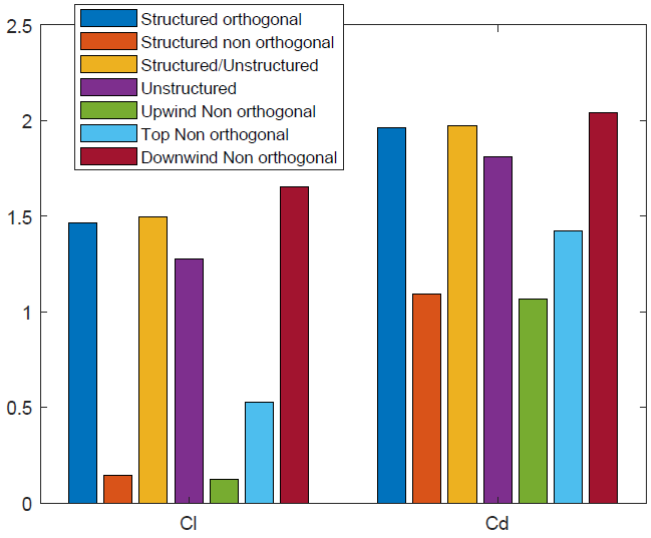


Figure 6.6: Maximum aerodynamic coefficients

Furthermor, in a histogram we plot the maximum values of lift and drag coefficients for all grids. In this figure (6.6), it is easier to see the differences between the meshes. As we have said before, *structured orthogonal* and *structured/unstructured* mesh obtain a very similar solutions. On the other hand, *structured non orthogonal*, *upwind non orthogonal* and *top non orthogonal*, which get a lower results. *Unstructured* grid have instead an acceptable result, even it is a little lower than the reference mesh.

Finally, we compute the relative error committed in the maximum values of the lift coefficient. For each case in the table 6.2, we store the percentage value of the relative error. Around 90% is the percentage error committed by the *structured non orthogonal* and *upwind non orthogonal*. A very high value which can not be neglected. observe that the unstructured mesh has the highest value of the relative error, followed by the structured non orthogonal mesh. Even the *top non orthogonal* grid have a high value (around 64%) of relative error, while the other grids have acceptable estimation.

$$\varepsilon(\%) = \frac{|\tilde{C}_L(orthogonal) - \tilde{C}_L(grid_i)|}{\tilde{C}_L(orthogonal)} \cdot 100 \tag{6.3}$$

| Mesh | $\varepsilon(\%)$ |
|---|---|
| Structured Orthogonal | - |
| Structured Non orthogonal | 90.08 |
| Structured/Unstructured | 2.22 |
| Unstructured | 12.97 |
| Structured Downwind Non orthogonal | 12.65 |
| Structured Upwind Non orthogonal | 91.36 |
| Structured Top Non orthogonal | 63.95 |

Table 6.2: Relative error of lift coefficient

## 6.2 Pressure distributions

The *pressure coefficient* is another important variable that can be evaluated. It is related to the aerodynamic forces. As it is shown in Fig. 6.7, around the top half of the cylinder surface, we analyze the variations of *mean pressure coefficient* and *RMSE static pressure coefficient*, respectively, $\bar{C}_p$ and $C_{p_{rms}}$.

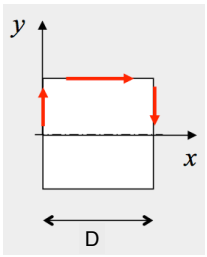


Figure 6.7: Cylinder surface scheme

To get the results of these variables, only one period is simulated, making sure of start in $C_L = 0$ and $\partial C_L/\partial t > 0$. Keeping the same time step, $\Delta t = 0.02$, the number of iterations are modified beacuse the period $T$, for each case, changes.

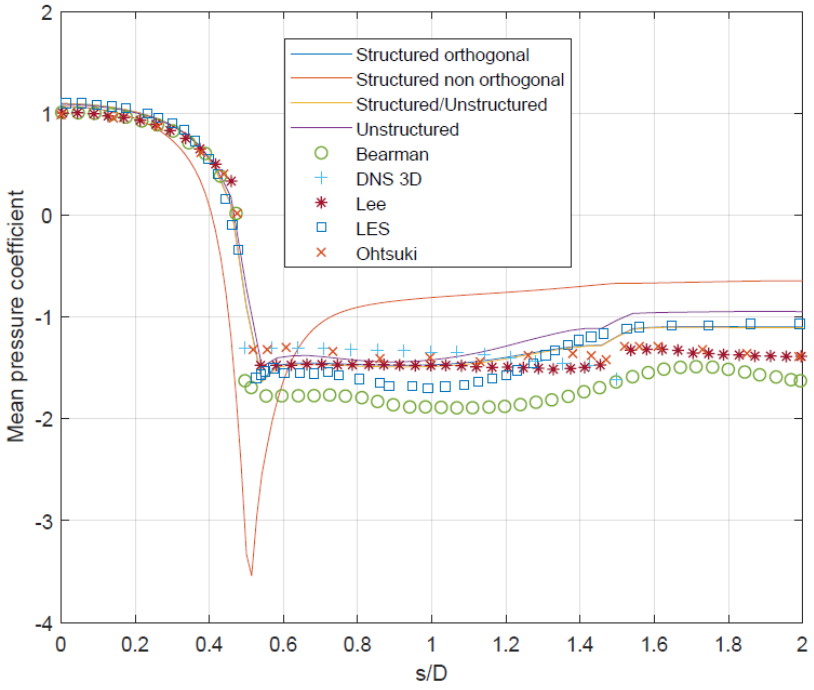


Figure 6.8: Mean pressure coefficient, $\bar{C}_p$

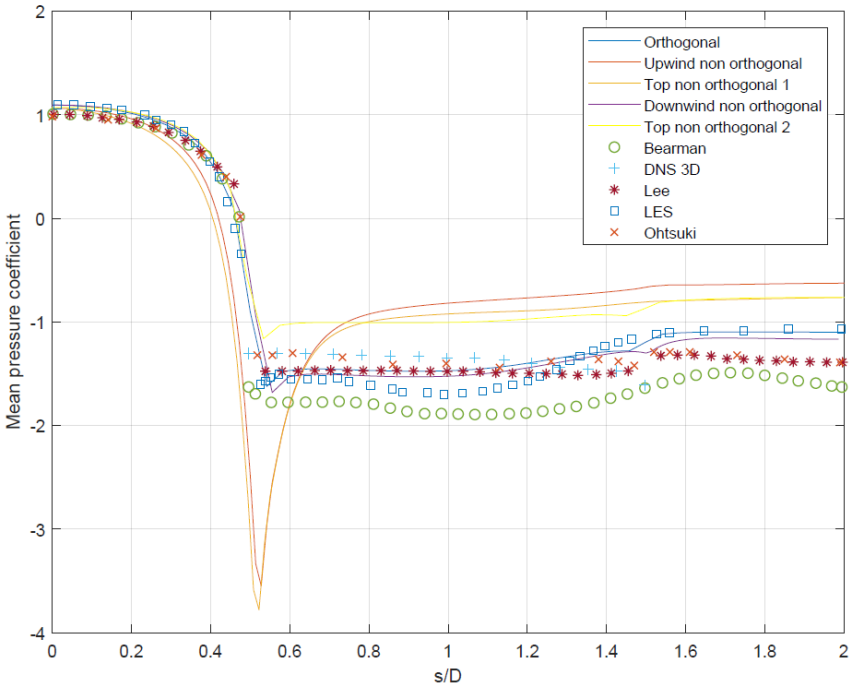


Figure 6.9: Mean pressure coefficient, $\bar{C}_p$

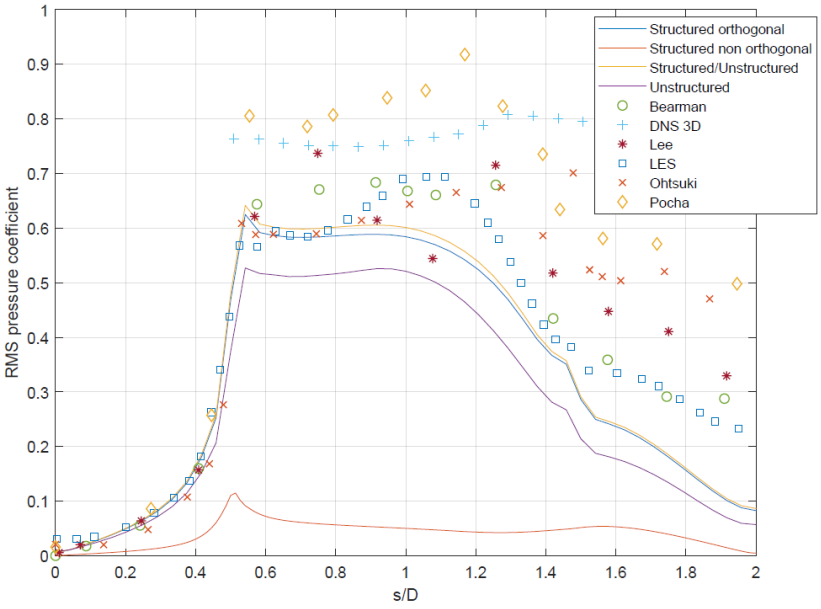


Figure 6.10: RMSE static pressure coefficient, $C_{p_{rms}}$

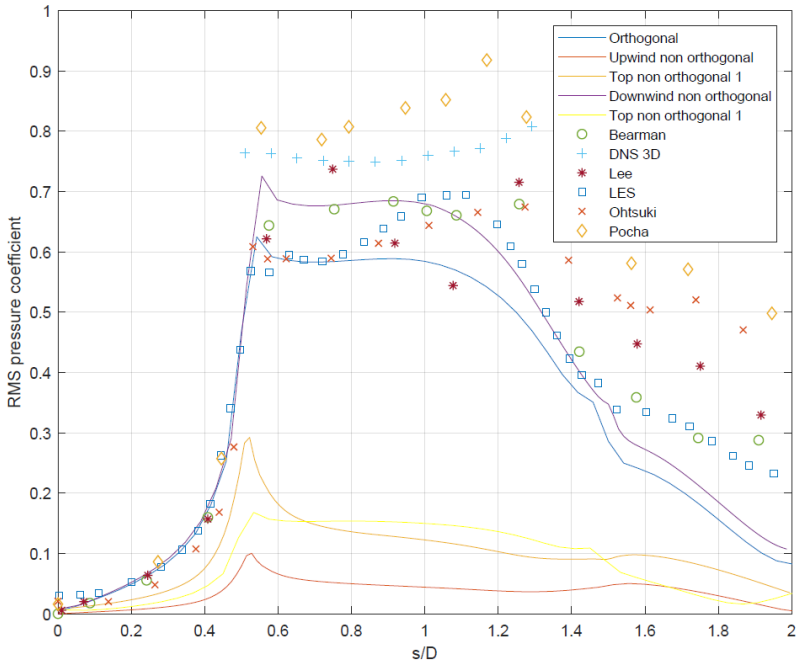


Figure 6.11: RMSE static pressure coefficient, $C_{p_{rms}}$

In the Fig. 6.8 and 6.9, it can be noticed that the *mean preassure coefficient* for the *structured/unstructured*, *unstructured* and *downwind non orthogonal* mesh is very similar to the results obtained from the reference mesh, the *structured orthogonal* grid. In addition, these results are near enough to the experimental data gathered from the literature. On the other hand, the *structured non orthogonal* and *upwind non orthogonal* meshes underestimate the *mean pressure coefficient* before $s/D = 0.5$, while after this positions, the results are overestimated. However, we can see two different values about the TOP NON ORTHOGONAL mesh, beacuse the grid is not symmetric. This leads to have different results in the upper and down zones of the cylinder. The results for the upper cylinder, where the grid is not orthogonal (in legend *top non orthogonal 1*), is similar to the *structured non orthogonal* and *upwind non orthogonal*. While the results obtained for the down case are similar to the bibliography data before $s/D = 0.5$, but after this position overestimate the experimental data. In all cases, in the stagnation point, located in the frontal face, the maximum $\bar{C}_p$ is gained, i.e. 1, while it is obtained negative values of *mean pressure coefficient*.

Finally, the *RMSE static pressure coefficient*, i.e. the root-mean-square error of $C_p$, is analyzed. As in the *mean pressure coefficients* case, in the Fig. 6.10 and 6.11, it can be noticed that the results of $C_{p_{rms}}$ about the *structured/unstructured*, *unstructured* and *downwind non orthogonal* meshes are close enough to the solutions of the *structured* mesh and literature data. On the other hand, the *structured non orthogonal*, *upwind non orthogonal* and both cases about the *top non orthogonal* grids underestimate a lot the values of $C_{p_{rms}}$ on the total half cylinder surface.

## 6.3 Wake flow

In this section we will analyze the *mean velocity in the x direction*, $\bar{u}_x$, along the line $y = 0$, which divides the square cylinder into two equal parts. Next, we will plot the stremlines and the instantaneous vorticity when LIFT COEFFICIENT has maximum value and, last but not least, the *mean velocity in the y direction* along lines $x = -0.25$, $x = 0$, $x = 0.25$ and $x = 0.5$. This last quantity is inspired by Fig. 2.8 from *Cao and Tamura*, [15].

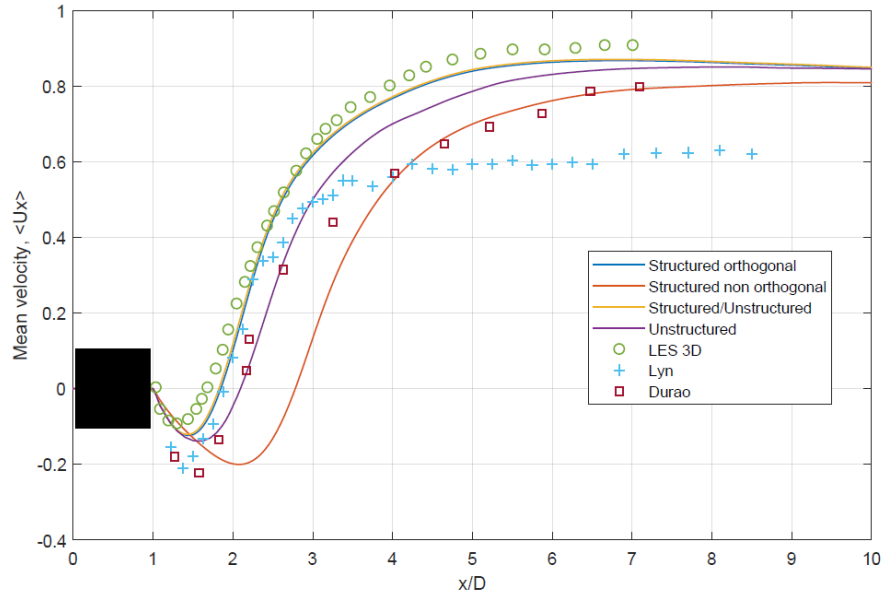


Figure 6.12: Mean velocity in the x direction, $\bar{u}_x$

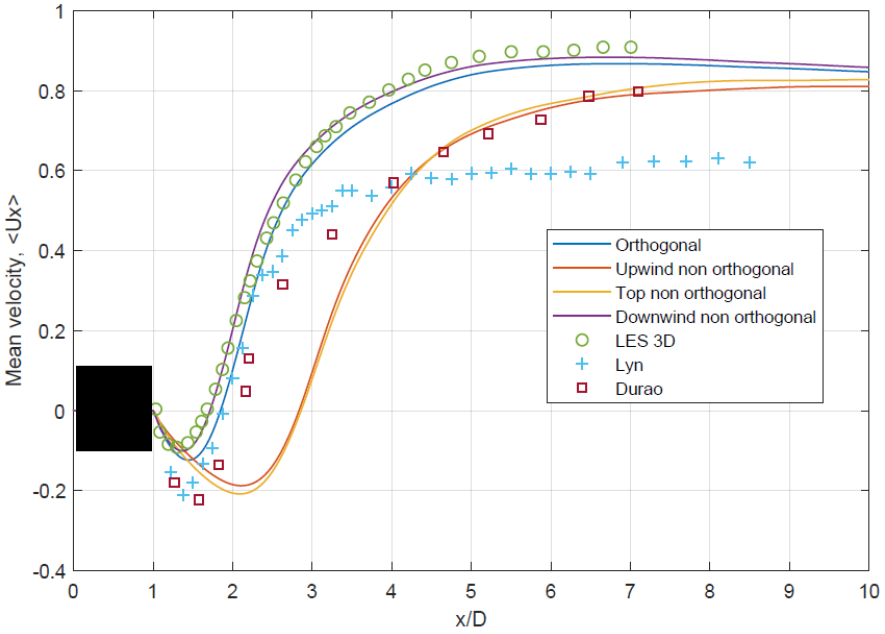


Figure 6.13: Mean velocity in the x direction, $\bar{u}_x$

In Fig. 6.12 and 6.13 there are plotted the data of *mean velocity in the x direction* about each grid. In addition, the data, included the bibliography, are saved until $x/D = 10$. As it was shown in all previous figures, the results provided by the *structured/unstructured*, *unstructured* and *downwind non orthogonal* meshes are very similar to the reference grid (*structured orthogonal* mesh) and literature data. In all cases, it can be noticed that the curves firstly decrease to increase later until a maximum. However, for each mesh, this evolution occurs in different points. One of the discrepancies that stands out is in the portion of space where the velocity is negative. In practical terms, the regions where the flow is reversed are completely different between the group of *structured non orthogonal*, *upwind non orthogonal* and *top non orthogonal* meshes and the other grids. In addition, the maximum value of $\bar{u}_x$ for the first group of grids is lower too than the others. All of this could lead to wrong conclusion about the physics of the simulated problem. This is also confirmed by the velocity profiles at vertical lines, Fig. 6.14-6.15, the same type of pictures from *Cao and Tamura* (Fig. 2.8), [15]. We can see that, at the line $x = 0.25$ and $x/D = 0.5$, no negative values are present in the flow about *structured non orthogonal*, *upwind non orthogonal* and *top non orthogonal* meshes. Moreover, at line $x/D = 0$, a strange behaviour affects this bad group of grids: the amount of mean velocity is totally different from the other meshes in the beginning of the vertical position. We can suppose that this is due to the non separation of the boundary layer, which leads to have still high values at the proximity top of the cylinder. This is also prove by the two different features of the *top non orthogonal* mesh. The flow at the negative y position, which is not affected by the skewness error, is rebaltated in positive position in order to reveal the asymmetry of the grid. In fact, the mean velocity is similar to the "good" meshes. Finally, at line $x/D = -0.25$, all grids have similar features instead.

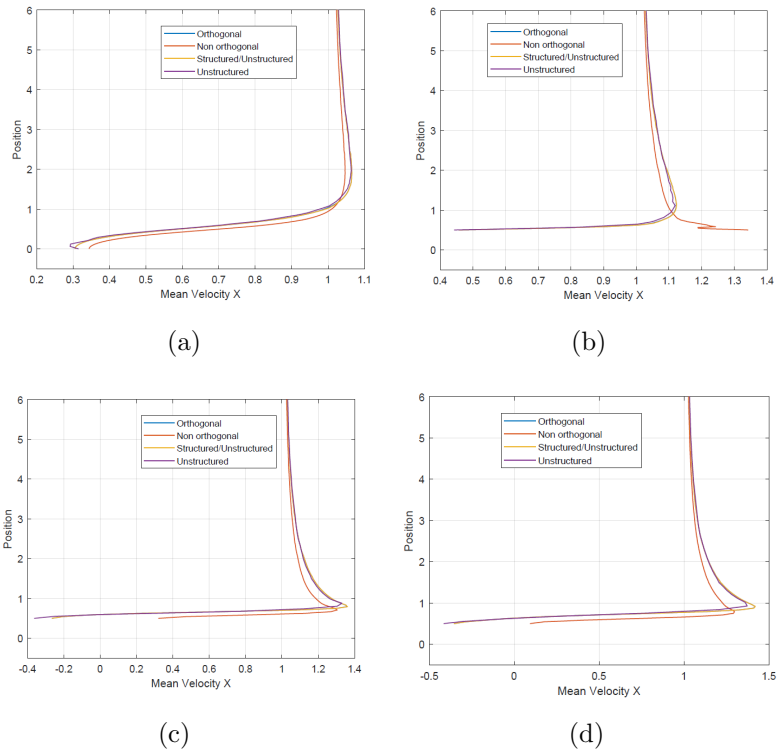


Figure 6.14: Mean velocity profiles along the vertical when $x/D = -0.25$ (a), $x/D = 0$ (b), 0.25 (c), 0.5 (d) for structured orthogonal, non orthogonal, structured/unstructured and unstructured grid

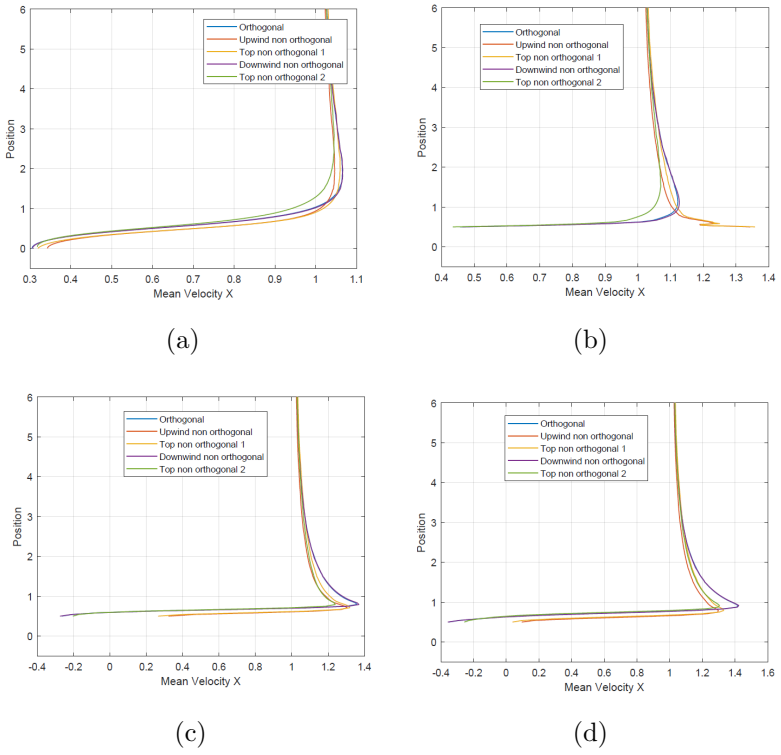


Figure 6.15: Mean velocity profiles along the vertical when $x/D = -0.25$ (a), $x/D = 0$ (b), 0.25 (c), 0.5 (d) for structured orthogonal, downwind non orthogonal, upwind non orthogonal and top non orthogonal grid

At this point, the suspect that the boundary layer is not well separated for *structured non orthogonal*, *upwind non orthogonal* and *top non orthogonal* is plausible. So, it is useful to analyze the streamlines and the instantaneous vorticity when lift coefficients value is maximum for each grid. In Fig. 6.16 we have plotted these results for each grid. Then, our considerations are confirmed: the flux is not separate at the boundary layer for these grids. From the vorticity contours, it can be noticed that the intensity of this value are much lower than other grids. Moreover, for *top non orthogonal* mesh, in the down zone of the cylinder, the flux is separated instead, while in the upper region of the cylinder is not separated. The only difference between the two zones is the mesh orthogonal and not orthogonal. Another demonstration that can be a correlation between a quality mesh and accurate solutions.

(a) Structured orthogonal

(b) Structured non orthogonal

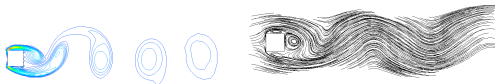

(c) Structured/Unstructured

(d) Unstructured

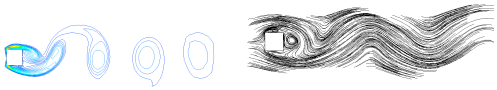

(e) Structured downwind non orthogonal

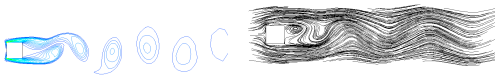

(f) Structured upwind non orthogonal

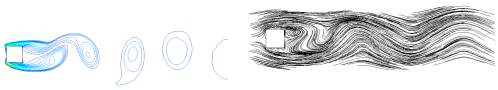

(g) Structured top non orthogonal

Figure 6.16: Streamlines and vorticity contours

## 6.4 Correlation Coefficients

In order to estimate a direct relation between skewness and error, we are going to compue a correlation coefficient and prove that this value is significant.

Firstly, we have to choose two grids to confrontate. A fine grid, in this case Structured Orthogonal, and a coarser grid that can be Structured Non Orthogonal, Upwind Non Orthogonal or Top Non Orthogonal. These are the grids in which the results are so many different from the others.

Secondly, we have to compute in the Inner Grid region the difference between the two grid chosen of the cell equiangle skewness and the gradients of flow field of velocity. With Fluent we can be easily obtain the values of these quantities in each grid. However, we can not calculate the differences between the two grid chosen beacuse the nodes of each grid are different. So, with Matlab, we interpolate the values of cell equiangle skewness and grandients velocity in the same equispaced grid. In this way, the computation of the differences is provided.

Thirdly, a measure of a quantity that describe the gradients velocity is needed to calculate. In fact, the gradients velocity are four, $\frac{\partial v_x}{\partial x}$, $\frac{\partial v_x}{\partial y}$, $\frac{\partial v_y}{\partial x}$, $\frac{\partial v_y}{\partial y}$. These values describe a Jacobian matrix of the flow field velocity. We choose the euclidean norm of this matrix as measure to represent the gradients velocity.

Then, we have all ingredients in order to calculate a correlation coefficient. However, the first results are not so fine. In fact, the data are so many noisy (6.17) and the linear correlation coefficient are near to zero. This is not what we expect. There are several reason for this fact. First, the cell equiangle skewness are not a reliable metric for the skewness. Another reason is that the inner ring is a region too big to capture a direct relation between skeness and error. The noisy data can be produced beacuse the error is propagate from the convective flux in zones where the skewness differences are small. Hence, we can try to localize only the region in which the skewness difference are higher. So, we choose the top part of the upwind zone of the inner ring to compute a correlation coefficient. This time the results are much better than before. With the help of the logaritmic transformations, the correlation is now near to 0.35, a moderate correlation between the skewness and the error. However, as we have already explained in section 4.1, we have to keep in mind that this measure is not reliable. In addition, we compute linear correlation coefficients while the data features are not linear. It is needed a rigorous statistical method to compute correctly a correlation coefficient. So, due to all the approximations both in the model and in the logical steps taken, it could not be considered a real statistical correlation, but more a kind of bulk measure of the link between the involved variables.

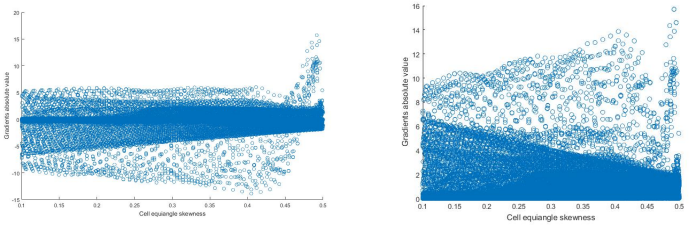


(a) (b)

Figure 6.17: Scatterplot of cell equiangle skewness and gradients (a), with absolute value in (b)

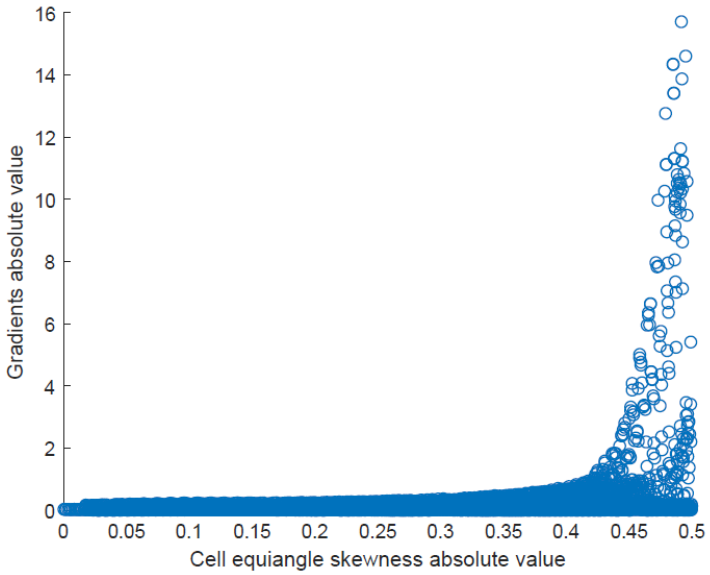


Figure 6.18: Scatterplot of cell equiangle skewness and gradients in absolute value

# Chapter 7

# Conclusion

*Computational Wind Engineering* has improved a lot in the last decades. There are many advantages in terms of time and cost of the simulations rather than expensive experiments. However, we should pay attention during the building of the model. An inappropriate definitions of the turbulence model, or the wrong numerical scheme chosen can have a strong impact on the solution. Overall, the construction of an inappropiate mesh is one of the most common errors. So, there are many methods to improve the mesh quality in order to avoid errors due to the inappropriate grids.

In this Thesis, the aim is to investigate about the effect of a poor mesh quality on the result. The local differences in quality between the grids used to run the same simulation can have a strong impact on the results. Starting from a local analysis of the involved forces, in terms of $C_L$, $C_D$ and $C_p$, a local source of error has been highlighted. Then, analyzing the streamlines and the vorticity contours, we have noticed that the flux is not separated at the boundary layer in cases of *structured non orthogonal*, *upwind non orthogonal* and *top non orthogonal*. In addition, inspection of velocity in the wake has shown that the error due to poor grid quality, that was supposed to be local, affects the quality of the solution even far away downstream from the body.
After some logical steps, a moderate correlation between skewness and variation of velocity has been founded. However, we recall that cell equiangle skewness is not a reliable measure of skewness. So, our estimation of linear correlation coefficient is not rigorously computed, but it is undeniable that a local error has been introduced by the difference between the several grids. For future works we suggest to find a reliable measure of skewness that can be computed, so that a rigorous correlation can be found in order to prove a direct relation between skewness and inaccurate solutions.

In conclusion, all that has been discussed in this Thesis is not just theoretical, but can have a wide range of applications. A typical subject of interest in *computational wind engineering* is the simulation of the wind flow behind a tall building. If a wrong simulation is run, then two kind of errors are introduced. The mistaken estimate of the $C_D$ can lead to underestimate the structural response of the building, and consequences in terms of safety are obvious. On the other hand, the misleading results on the nature of the flux, as we have seen in *mean velocity in the x direction* values along line $y = 0$, can have unpleasant consequences in terms of urban comfort. If the flow is actually reverse,

while simulation suggests the opposite, then a pollutant dispersed in the wake could be directed towards the rear face of the building, causing a discomfort not predicted by the model, or a waste of money for an urban comfort installation built in the wrong place.

# Bibliography


[1] H. Jasak. *Error Analysis and Estimation for the Finite Volume Method with Applications to Fluid Flows*. Ph.D. for Mechanical Engineering, University of London and Imperial College of Science, Technology and Medicine, 1996.

[2] L. Bruno, D. Fransos, N. Coste and A. Bosco, "3D flow around a rectangular cylinder: A computational study." *Journal of Wind Engineering and Industrial Aerodynamics*, 98: 263-276, 2010.

[3] L. Bruno, Maria V. Salvetti and F. Ricciardelli, "Benchmark on the Aerodynamics of a Rectangular 5:1 Cylinder: An overview after the first four years of activity." *Journal of Wind Engineering and Industrial Aerodynamics*, 126: 87-106, 2014.

[4] T. J. Chung, *Computational Fluid Dynamics*, Cambridge University Press, 2002

[5] J.Blazek, *Computational Fluid Dynamics: Principles and Applications*, Elsevier, 2001

[6] Abdulnaser Sayma, *Computational Fluid Dynamics*, Ventus Publishing ApS, 2009

[7] F. Moukalled, L. Mangani, M. Darwish, *The Finite Volume Method in Computational Fluid Dynamics*, Springer, 2016

[8] H. Ye, D. Wan, *Benchmark computations for flows around a stationary cylinder with high Reynolds numbers by RANS-overset grid approach*, Applied Ocean Research 65: 315326, 2017

[9] G. F. Rosetti, G. Vaz, *On the numerical simulation of captive, driven and freely moving cylinder*, Journal of Fluids and Structures, 74: 492519, 2017

[10] Y. Kallinderis, C. Kontzialis, *A priori mesh quality estimation via direct relation between truncation error and mesh distortion*, Journal of Computational Physics 228: 881902, 2009

[11] S. Fotia, Y. Kallinderis, *Quality index and improvement of the interfaces of general hybrid grids*, Procedia Engineering, 82: 416427, 2014.

[12] B. Blocken, "50 years of Computational Wind Engineering: Past, present and future", *Journal of Wind Engineering and Industrial Aerodynamics*, 129: 69102, 2014.

[13] Gang Hu, K.T. Tse, K.C.S. Kwok, Yu Zhang, "Large eddy simulation of flow around an inclined finite square cylinder", *Journal of Wind Engineering and Industrial Aerodynamics*, 146: 172-184, 2015.

[14] R. Fattah, D. Angland and X. Zhang, "A priori grid quality estimation for high-order finite differencing", *Journal of Computational Physics*, 315: 629-643, 2016.

[15] Y. Cao and T. Tamura. Large-eddy simulations of flow past a square cylinder using structured and unstructured grids. *Computers and Fluids*, 137: 36-54, 2016.

[16] John H. Ferziger and M. Perić. *Computational Methods for Fluid Dynamics*. Springer, Berlin, 3rd edition, 2002.

[17] John D. Anderson Jr. *Fundamentals of Aerodynamics*. McGraw-Hill Series in aeronautical and aerospace engineering, New York, 3rd edition, 2001.

[18] FLUENT 6.3 User's Guide

[19] ANSYS FLUENT 12.0 User's Guide

[20] D. Fransos, *Stochastic Numerical Models for Wind Engineering*. Ph.D. in Mathematics for Engineering Sciences, Politecnico di Torino, 2008.

[21] Ichiro Nakane, *Effectiveness of Grid Orthogonality on Body Fitted Curvilinear Coordinate System in CFD*,International Journal of Environmental Science and Development, Vol. 4, No. 2, April 2013

[22] Almudena López Sanfeliciano, *Computational Study of the Numerical Effects caused by the Mesh Quality in a Square Cylinder*. Master Degree in Aerospace Engineering, Politecnico di Torino, 2017

[23] L. Bruno, *Lezione Griglie di calcolo: generazione, qualit e adattamento.*, Lecture notes of Computational Fluid Dynamics and Wind Engineering course, Politecnico di Torino, 2014